

CALIFORNIA STATE UNIVERSITY, NORTHRIDGE

The Rheological Evolution of Brittle-Ductile Transition Rocks During the Earthquake
Cycle: Evidence for a Plastic Precursor to Pseudotachylyte in an Extensional Fault
System, South Mountains, Arizona

A thesis submitted in partial fulfillment of the requirements
For the degree of Master of Science in Geology

By
Craig Stewart

May 2017

The thesis of Craig Stewart is approved:

Dr. Doug Yule

Date

Dr. John Platt

Date

Dr. Julian Lozos

Date

Dr. Elena Miranda, Chair

Date

California State University, Northridge

Acknowledgements

It has become clear to me that this degree was not a solo endeavor. That I truly stand on the shoulders of giants, not only in my scientific field but in my life. I am truly blessed by all of my mentors and friends who have become too numerous to name. I respect, admire, and value your presence in my life.

I wish to acknowledge the California State University Northridge (CSUN) Department of Geological Sciences for their support of this research, as well as Marilyn Hanna for her contributions to our research and lab. Additional gratitude goes to those who have taught me the concepts of which my science is based, and also to those who discussed concepts with me as we strove to push the envelope. Dr. Jamie Levine, Dr. Gabriele Casale, Dr. Whitney Behr, Dr. John Platt, Dr. Julian Lozos, Dr. Doug Yule, Dr. Dick Heermance among many others helped me build the foundation of these ideas.

Without the knowledge, collaboration, and wisdom provided by my advisor Dr. Elena Miranda I would not have the skills necessary to complete this project. Before I began graduate school I barely understood what the acronym EBSD stood for. Look at me now! I owe much of my new understanding of microtectonics and rheology to Dr. Miranda.

I have grown during my time at CSUN and attribute it to my mentors, but also to everyone who has been a part of my time here in California. However, I will never forget those who are a short 2500 mile road trip away in North Carolina, thank you.

Table of Contents

Signature page.....	ii
Acknowledgements.....	iii
List of Tables	vi
List of Figures.....	vii
Abstract.....	viii
Chapter 1: Introduction.....	1
Chapter 2: Geologic Setting.....	4
Chapter 3: Methods.....	7
3.1 Field Work	7
3.2 Light Microscopy.....	7
3.3 EBSD	8
Chapter 4: Results.....	12
4.1 Field Observations	12
4.2 Microstructures with Light Microscopy	13
4.2.1 Microstructures in control mylonite.....	13
4.2.2 Microstructures of host mylonites to pseudotachylytes	14
4.2.3 Microstructures of pseudotachylyte veins.....	14
4.3 EBSD	16
4.3.1 Microstructures in control mylonite,	16
0.3 μm step size	
4.3.2 Microstructures within host mylonites to pseudotachylytes,	20
0.75 μm step size	
4.3.3 Microstructures of survivor clasts,	24
0.3 μm step size	
4.4 Piezometry	29
Chapter 5: Discussion	31
5.1 Deformation of Quartz and Feldspars.....	31

5.2 Quartz LPO Evolution and Deformation Mechanisms.....	32
5.3 Rheological Evolution during the Earthquake Cycle.....	35
Chapter 6: Conclusions	43
References.....	45
Appendix A: Local misorientation maps	51

List of Tables

Table 1: Scanning electron microscope working conditions	9
Table 2: Grain size data calculated from EBSD	30

List of Figures

Figure 1: Schematic diagram of crustal stress transfer	2
Figure 2: Geologic map of study area.....	4
Figure 3: Field photos	13
Figure 4: Microphotographs of processed samples	15
Figure 5: EBSD of control mylonite sample 08-02	18
Figure 6: EBSD of host mylonite sample 2-7-1.....	19
Figure 7: EBSD of host mylonite sample 3-5B	23
Figure 8: EBSD of survivor clasts	26
Figure 9: EBSD of pseudotachylyte	29

Abstract

The Rheological Evolution of Brittle-Ductile Transition Rocks During the Earthquake Cycle: Evidence for a Plastic Precursor to Pseudotachylyte in an Extensional Fault System, South Mountains, Arizona

By

Craig Stewart

Master of Science in Geology

We investigate how the rheological evolution of shear zone rocks from beneath the brittle-ductile transition (BDT) is affected by coeval ductile shear and pseudotachylyte development associated with seismicity during the earthquake cycle. We focus our study on footwall rocks of the South Mountains core complex, and we use electron backscatter diffraction (EBSD) analyses to examine how strain is localized in 3 granodiorite mylonites both prior to and during pseudotachylyte development beneath the BDT. In mylonites that are host to pseudotachylytes, deformation is partitioned into quartz, where quartz exhibits lattice preferred orientation patterns and microstructures indicative of dynamic recrystallization during dislocation creep. Grain size reduction during dynamic recrystallization leads to the onset of grain boundary sliding (GBS) accommodated by fluid-assisted diffusion creep, localizing strain in quartz-rich layers prior to pseudotachylyte development. The close association of foliation-parallel zones of GBS in

the mylonites, and the overwhelming presence of GBS traits in polycrystalline quartz survivor clasts indicate that GBS zones were the plastic precursors to *in situ* pseudotachylyte generation. During pseudotachylyte development, strain was partitioned into the melt phase, where grain size sensitive flow continued until crystallization impeded flow. Grain size piezometry shows high differential stress values in both host mylonites (~160 MPa) and pseudotachylytes (> ~200 MPa), consistent with high stresses expected for interseismic and coseismic deformation. The multiple veins of co-planar pseudotachylyte indicates a cyclicity to their development, but their lateral discontinuity suggests that the seismic events are confined to the deep crust, consistent with characteristics of deep crustal tremor. Our findings indicate that pseudotachylytes with plastic precursors may be produced during slower-slip seismic events, and can be used to identify former tremor events in the deep crust.

Chapter 1: Introduction

The brittle-ductile transition (BDT) defines a long-term, average depth below which earthquakes are purportedly rare, yet there is a growing body of evidence that indicates considerable amounts of seismic behavior beneath the BDT (e.g., Rowe and Griffith, 2015). The presence of pseudotachylytes in rocks beneath the BDT is probably the best-known example of this evidence, where pseudotachylyte formation is commonly explained by stress transfer between a discrete fault above the BDT and its down-dip continuation as a distributed shear zone beneath the BDT. In this traditional ‘top-down’ model, an earthquake below the long-term average BDT temporarily displaces the BDT downward, imparting brittle failure into crust that was previously deforming plastically (Figure 1). The coseismic release of stress into the layer between the long-term and displaced BDT (i.e., the ‘schizosphere’) loads the underlying ‘plastosphere’, which responds by inducing flow that promotes subsequent rebound of the BDT back through the schizosphere during postseismic creep (Scholz, 2002). However, this origin for pseudotachylyte is inconsistent with the recent compilation of crustal strength measurements that indicates that brittle faults are weak, and may not be able to transfer stresses downward through the BDT owing to the considerable strength of the ductile crust (Behr and Platt, 2014). A ‘bottom-up’ model of stress transfer is proposed here, where in situ and coeval pseudotachylytes develop within otherwise ductile mylonites owing to a plastic precursor developed during the seismic cycle (Figure 1). Our ability to assess the rheology of pseudotachylyte-bearing rocks beneath the BDT in the context of the earthquake cycle is compromised by our incomplete understanding of how pseudotachylyte is generated beneath the BDT and the apparent paucity of deep crustal pseudotachylytes

that are preserved in the geologic record (e.g., White, 2012; Kirkpatrick and Rowe, 2013; Rowe and Griffith, 2015).

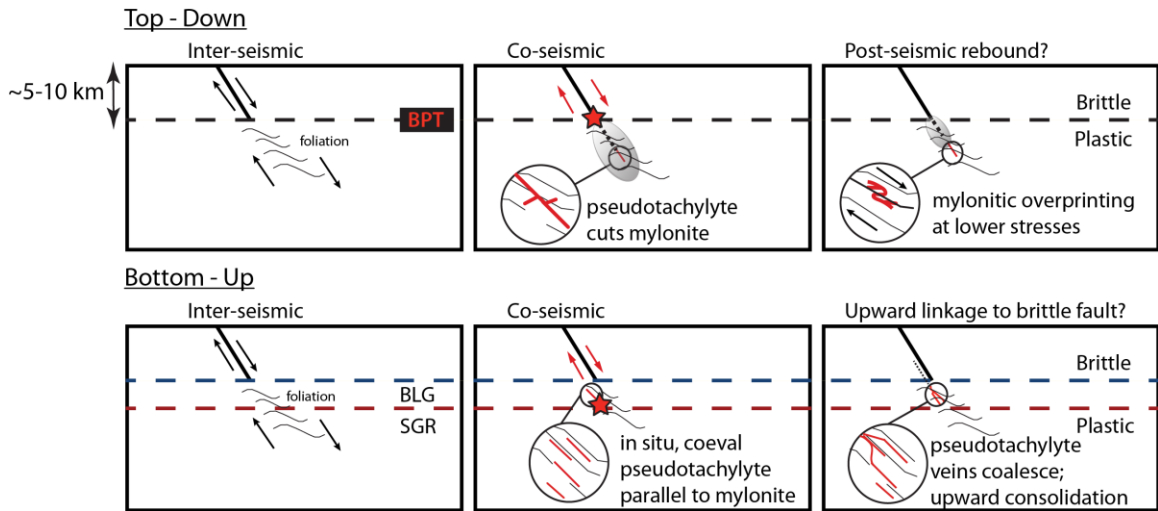


Figure 1: Two schematic models of pseudotachylyte development in the South Mountains of Arizona. A ‘top-down’ schematic model (above) where brittle rupture in the seismogenic zone penetrates the BPT resulting in pseudotachylyte cross cutting the mylonitic fabric, and then being reworked during post seismic relaxation. A proposed ‘bottom-up’ schematic model (below) where rheologic weakening allows for pseudotachylyte generation parallel to foliation as the footwall denudes out of the plastosphere possibly connecting to an overlying weak brittle fault system.

The extensional fault systems known as metamorphic core complexes are tectonic windows into the crust beneath the BDT (e.g., Platt et al., 2014), and young core complexes in particular offer the best opportunity to preserve deep crustal pseudotachylytes due to the rapid exhumation and cooling of young footwall rocks. In this study, we examine mylonite-hosted pseudotachylyte samples from the footwall of the South Mountains metamorphic core complex (SMCC) in Arizona to evaluate deformation associated with the earthquake stress cycle. The SMCC is uniquely appropriate for this study because the footwall rocks 1) contain direct evidence for earthquakes beneath the BDT (e.g., pseudotachylytes within mylonites) (Goodwin, 1999), 2) preserve diagnostic microstructures of the earthquake cycle because they were rapidly cooled ($>200^{\circ}\text{C}/\text{my}$) during exhumation (Linder, 2015), and 3) record a simple tectonic history where a mid-Miocene composite pluton was

subsequently deformed by an extensional detachment fault system during a single episode of mid-Miocene extension (Reynolds, 1985; Reynolds et al., 1986; Smith et al., 1991).

We analyze pseudotachylyte-bearing mylonites and a ‘control’ mylonite distal to the pseudotachylytes to demonstrate that high stress conditions accompanied interseismic deformation and helped promote the onset of grain boundary sliding prior to pseudotachylyte development. We argue that highly localized zones of grain boundary sliding were the precursors to pseudotachylyte development, and that interseismic peak stresses are recorded by the pseudotachylytes during coseismic deformation. We discuss the importance of fluid-enhanced GBS in creating instabilities that lead to coeval pseudotachylyte and mylonite development, and we suggest that these particular types of pseudotachylytes may represent recurring tremor events below the BDT.

Chapter 2: Geologic Setting

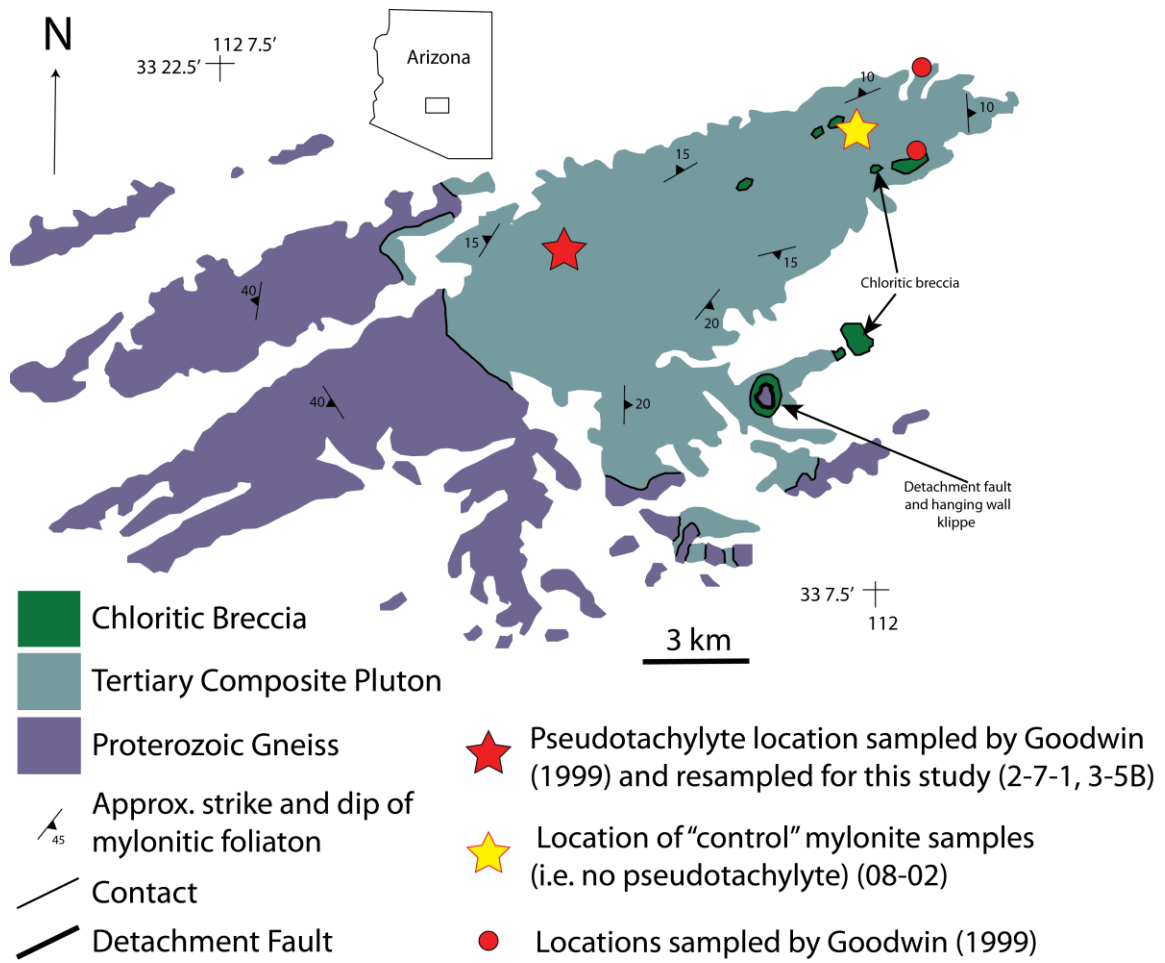


Figure 2: Simplified geologic map of South Mountains basement rock adapted from Goodwin (1999) indicating sampled pseudotachylyte locations and the location of the preserved detachment fault.

The South Mountains metamorphic core complex (SMCC) is the geologically simplest of the core complexes of the western North American Cordillera. Proterozoic rocks are intruded by a composite mid-Miocene pluton that was subsequently deformed by a mid-Miocene extensional detachment fault system as it was crystallizing, and all deformation fabrics in the plutonic rocks are attributed to this single episode of mid-Miocene extension (Reynolds, 1985; Reynolds et al., 1986; Smith et al., 1991) (Figure 2). The composite pluton is dominantly composed of granodiorite with lesser amounts of

granite and alaskite, where Rb-Sr, U-Th-Pb, and K-Ar techniques suggest crystallization of the suite at ~25-22 Ma (Reynolds, 1985; Reynolds et al., 1986). The composite pluton was variably deformed by high-temperature (400-600° C) mylonites (Reynolds, 1985; Smith et al., 1991; Greenberg, 2010; Annis, 2012) in an extensional ductile shear zone that was kinematically continuous with and down-dip of the brittle detachment fault (Davis et al., 1986). The extensional deformation is bracketed between 20.6 +/- 0.37 and 19.4 +/- 0.27 Ma based on U-Pb zircon LA-ICPMS dates from the composite pluton and from cross-cutting dikes (Clements, 2013). The mylonites were rapidly exhumed from at or below the BDT during extension along the detachment fault (Davis et al., 1986; Fitzgerald et al., 1993), where the fast cooling rate (> ~200°C/m.y.) (Fitzgerald et al., 1993; Linder, 2015) suppressed annealing and resulted in impeccable preservation of microstructures. The relatively young BDT rocks of the SMCC therefore lack a complicated tectonic history, and their deformation fabrics preserve details of BDT rock rheology during a single extensional event.

The pseudotachylyte-bearing SMCC mylonites were exhumed from beneath the BDT during extensional detachment faulting in the Middle Miocene. Microstructural observations (Reynolds, 1985; Goodwin, 1999; Greenberg, 2010; Annis, 2012) and stable isotope data (Smith et al., 1991) indicate that mylonitic fabrics developed over a temperature range of ~400 – 600° C. These temperatures are higher than the temperature threshold associated with the BDT in typical continental crust (~300 +/- 50° C) (e.g., Kohlstedt et al., 1995; Scholz, 2002), indicating that the SMCC mylonites developed beneath the BDT. However, the BDT was likely to be relatively shallow (5-10 km) during detachment faulting due to the high geothermal gradient associated with intrusion of the

composite pluton that is host to the mylonites (Livaccari et al., 1995). The SMCC mylonites were therefore formed beneath a shallow BDT, and of critical importance for our study is that they are host to multiple generations of pseudotachylytes that also formed near or below the BDT (Goodwin, 1999). This latter trait distinguishes the SMCC mylonites as ideal for our study as they record details of the earthquake cycle in rocks beneath the BDT.

Pseudotachylyte veins are closely associated with the mylonites, and are exposed in at least three mapped locations within the SMCC (Figure 2)(Goodwin, 1999). In all three locations, the pseudotachylyte is generally subparallel to mylonitic foliation, although it may also locally cross-cut mylonitic foliation (Goodwin, 1999). The pseudotachylyte veins range from being completely undeformed to variably mylonitized, indicating episodic formation both during and after mylonitic fabric development and minor subsequent crustal flow (Goodwin, 1999). We collected our samples from Dobbins Lookout in the central part of the complex, which is one of the regions sampled by Goodwin (1999) (Figure 2).

Chapter 3: Methods

3.1 Field work

The two main objectives of field work were to 1) observe the nature of the relationship between host mylonite and pseudotachylyte, and 2) collect samples of pseudotachylyte-bearing mylonites. We collected fifteen oriented samples of pseudotachylyte-bearing mylonites from Dobbins Lookout. We selected samples based on the presence of semi-continuous pseudotachylyte veins that are sub- to co-planar to the mylonitic foliation. In this paper, we present data from two of these pseudotachylyte-bearing samples and from a ‘control’ mylonite sample collected as part of an earlier study (Greenberg, 2010). The control mylonite (08-02) was collected from the northern side of the South Mountains main ridge, between the pseudotachylytes exposed at Dobbins Lookout and those exposed in the northeast portion of the range. We chose this location as it represents an area where the mylonitic fabric is similar in character to those host to pseudotachylyte, and is developed within the same granodiorite unit of the composite pluton host to the pseudotachylytes at Dobbins Lookout. Therefore, the control mylonite was used to observe mylonites not directly impacted by pseudotachylyte generation, but that otherwise would be at fairly equant structural depth to the detachment fault. We cut all samples perpendicular to mylonitic foliation and parallel to lineation in preparation for thin sectioning.

3.2 Light Microscopy

We used light microscopy to confirm the presence of pseudotachylyte, investigate the nature of the contacts between pseudotachylyte veins and their host mylonites, and

identify deformation microstructures within 1) the control mylonite, 2) the mylonites that are host to pseudotachylytes, and 3) the survivor clasts within pseudotachylyte veins. A secondary objective of light microscopy was to select areas for further microstructural work using Electron Backscatter Diffraction (EBSD). We optically analyzed a total of 3 thin sections in plane and cross-polarized light.

3.3 EBSD

We used EBSD analysis to 1) confirm the presence of deformation microstructures observed with light microscopy, 2) generate beam maps that resolve fine-scale microstructures and permit the measurement of grain size and aspect ratio, and 3) determine the crystallographic orientations of grains. Thin sections were ultrapolished in preparation for EBSD analyses and analyzed at California State University Northridge using an FEI Quanta 600 scanning electron microscope (SEM) equipped with an Oxford Instruments Nordlys EBSD detector and AZtec EBSD acquisition software. Samples were uncoated and analyzed under low vacuum conditions (20 Pa water) to minimize the charging effects of the electron beam.

We collected nine EBSD beam maps from three samples (08-02, 2-7-1, and 3-5B) for this study. The maps include 1) a high resolution (0.3 μm step size) map from a granodiorite control mylonite (sample 08-02), 2) a large map of host mylonite microstructures developed ~ 2 mm from a pseudotachylyte vein, (step size of 0.75 μm , sample 2-7-1), 3) a large map of the contact between host mylonite and a co-planar pseudotachylyte vein (step size of 0.75 μm , sample 3-5B), 4) three high resolution (0.3 μm step size) maps of polycrystalline quartz survivor clasts entrained in pseudotachylyte (samples 3-5B and 2-7-1), and finally 5) three large (step size 7 μm) maps of

pseudotachylyte in samples 3-5B and 2-7-1. The SEM and EBSD working conditions for each map are shown in Table 1.

Sample	sample type	size (μm)	step size (μm)	Accelerating voltage (kV)	spot size	filament current (A)	emission current (μA)	working distance (mm)	raw indexing rates of EBSD map (%)	raw indexing rates of mylonitic rock host to pseudotachylytes (%)	raw indexing rates of pseudotachylytes (%)
08_02	Control mylonite	200 x 100	0.3	25	7	2.1-2.35	99-102	14.1	96	N/A	N/A
2_7_1	Host mylonite	550 x 290 240 x 140	0.75	25	7	2.1-2.35	99-102	13.3	87	N/A	N/A
3_5B	Host mylonite	800 x 220	0.75	25	7	2.1-2.35	99-102	14.9	89	93	60
3_5B	Survivor clast	240 x 120	0.3	25	7	2.1-2.35	99-102	13.1	67	86	7
3_5B	Survivor clast	210 x 130	0.3	25	7	2.1-2.35	99-102	13.2	63	92	47
2_7_1	Survivor clast	280 x 60	0.3	25	7	2.1-2.35	99-102	15.3	84	90	66
3_5B	Pseudotachylyte	2254 x 1092	7	25	7	2.1-2.35	99-104	15.5	43	N/A	43
3_5B	Pseudotachylyte	2156 x 1127	7	25	7	2.1-2.35	99-104	15.1	43	N/A	43
2_7_1	Pseudotachylyte	2394 x 1176	7	25	6.5	2.1-2.35	99-104	15.3	64	N/A	64

Table 1: Samples are categorized by their identification number and associated texture. The size of each EBSD map, along with the active working conditions of the scanning electron microscope are provided with their appropriate units of measure including map size, step size, spot size, accelerating voltage, filament current, emission current, working distance, along with the raw indexing rates associated with mylonitic material and pseudotachylyte.

EBSD data were post-processed and noise-reduced using the Oxford Instruments hkl Channel 5 software suite. Noise reduction included the removal of wild spikes, which are defined as single pixels having a different orientation relative to their surrounding 8 neighbor pixels. Additional noise reduction included extrapolation of zero solutions to match their 8 or 7 neighbor pixels of same orientation.

We use the hkl Channel 5 Tango software to plot phase maps, average intragrain misorientation maps, and local misorientation EBSD maps. In each of these maps, we define grain boundaries as having $\geq 10^\circ$ of misorientation, and subgrain boundaries as having between 2-10° of misorientation. Phase maps classify minerals based on the indexing of crystallographic symmetries and discerns grains by neighbor misorientations.

We use phase maps to evaluate the spatial distribution and grain boundary relationships between individual and groups of mineral grains. Average intragrain misorientation maps assign colors to grains based on the average amount of crystal lattice misorientation per unit area within a grain. We use these maps as a proxy for relative amounts of intragrain crystal plasticity, and we subset populations of recrystallized grains that have low ($<2^\circ$) average intragrain misorientation. Local misorientation maps reveal the locations of low-angle misorientations (up to 5°) within grains, effectively highlighting both subgrain boundaries and the location of fine-scale intracrystalline deformation.

We use the high-resolution EBSD maps to measure grain diameters for paleopiezometry. We estimate our maximum errors in grain size measurement to be between 5 and 10% because the step sizes of the maps (0.75 and 0.3 μm) were chosen relative to the grain size to produce a minimum of 5 to 10 pixels per grain (Humphreys, 2001). Errors in Table 2 are representative of standard error in grain size propagated through the published error of the paleopiezometer. Only recrystallized quartz grains that are not adjacent to other phases were used for piezometry calculations. This filtering results in a conservative measurement that may under-sample grains that have grown under crystal plasticity. We use the Stipp and Tullis (2003) piezometric relationships to calculate the grain sizes of dynamically recrystallized quartz aggregates.

We plot quartz crystallographic orientation data in pole figures. Pole figures are plotted as lower hemisphere, equal area stereographic projections using the hkl Channel 5 Mambo software. The *c*-axis [0001] orientations of quartz are plotted in pole figures in reference to the foliation and lineation. Each pole figure plot shows one point per grain so as to not over-sample larger grains. Contouring is set at a 10 degree half width to provide

a conservative amount of smoothing to the contours. Multiples of uniform distribution (m.u.d.) provides a measure of the fabric strength in regards to crystallographic orientations and was pinned at 7 for each contoured pole figure displayed.

Chapter 4: Results

4.1 Field observations

Near Dobbins Lookout there is an abundance of pseudotachylyte, however, the veins are present only within a zone that is ~10 m in structural thickness, which is where our host mylonite and mylonitized pseudotachylyte samples were collected (2-7-1 and 3-5B). Most pseudotachylyte veins are oriented sub- to co-planar with the mylonitic fabric of the granodiorite and are <0.5 - 3 cm thick and laterally continuous for 0.5 - 1 m. The veins are sinuous in shape with distinct margins to the mylonite, but younger injection veins also cut the mylonitic fabric. Pseudotachylyte veins are not consistently planar as they locally conform to the dominant mylonitic fabric, and survivor clasts of the host mylonite entrained in the frictional melt material are visibly elongate parallel to foliation (Figure 3). The foliation is defined by an S-C-C' fabric with minerals generally elongate in the S direction. When looking down the stretching lineation, pseudotachylyte veins are locally cross-cut by C' fabrics. The control mylonite exhibits S-C fabric where both foliation and lineation are apparent, but the lineation is better developed relative to the foliation.

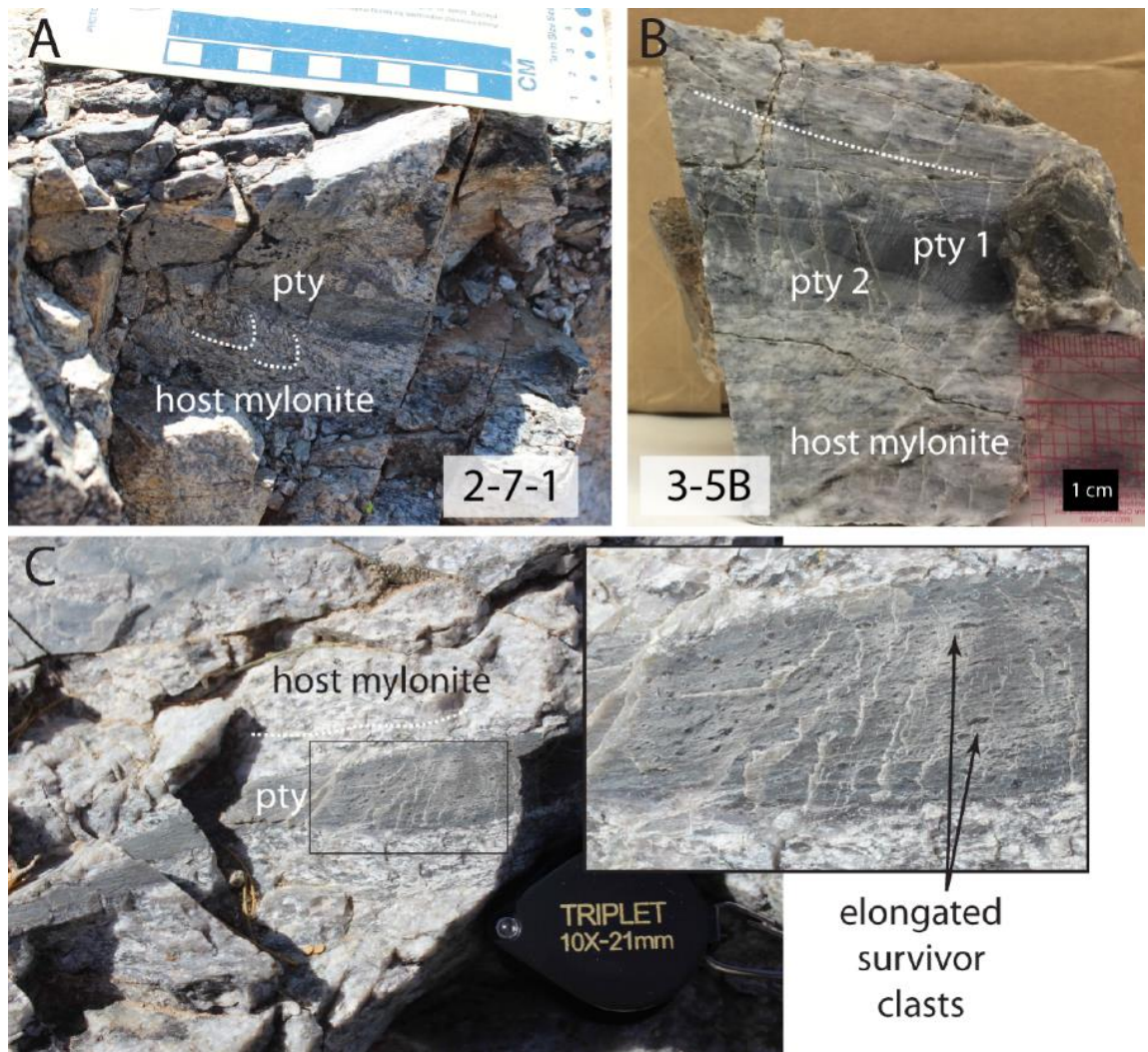


Figure 3: Annotated field and hand sample photos of host mylonite samples 2-7-1 and 3-5B. Local sample foliation in both photos is marked by white dotted lines. A) Field photo of host mylonite sample 2-7-1 with a local foliation that folds into the darker grey pseudotachylyte vein. B) Cut face of host mylonite sample 3-5B with two textures of pseudotachylyte within the same foliation sub-parallel vein. C) Field photo of unsampled host mylonite face where pseudotachylyte is dark grey compared to the surrounding granodiorite mylonite, and entrained survivor clasts are visibly elongate parallel to the vein.

4.2 Microstructures with light microscopy

4.2.1 Microstructures in control mylonite

The control mylonite has a well-developed anastomosing mylonitic foliation, with feldspar porphyroclasts and fine-grained biotite and quartz composing the matrix (Figure 4). Intragrain fractures are present within 15% of feldspar porphyroclasts. Quartz grains

are organized into elongate ribbons that are deflected and pinched around feldspar porphyroclasts, where grain size becomes more homogenous and decreases. Quartz grains away from porphyroclasts remain more variable in grain size and elongate in shape. Quartz grain boundaries are inequigranular and interlobate, with sinuous subgrain boundaries. Biotite fish and fine-grained mica aggregates are present along the S-C folia of the mylonite.

4.2.2 Microstructures of host mylonites to pseudotachylytes

The host mylonitic fabric is composed of feldspar porphyroclasts distributed through an anastomosing region of inequigranular, interlobate quartz grains and biotite fish. Locally the foliation is compositionally layered. Most feldspar porphyroclasts (>90%) within the mylonite are heavily fractured with either conjugate or imbricate intragrain fractures. Feldspar grain boundaries are variably serrated. Quartz grains are of variable size (<10 - ~100 μm) and form elongate ribbons. Quartz grain size decreases where ribbons are 'pinched' near feldspar porphyroclasts. Biotite is present along S-C planes within the mylonite but appears 'shredded' with a fine grain size.

4.2.3 Microstructures of pseudotachylyte veins

Pseudotachylyte of the South Mountains is variably mylonitized with elongate survivor clasts distributed throughout the veins (Figure 4). Sweeping extinction in microcrystalline biotite of the frictional melt material is visible in cross-polarized light. Over 90% of survivor clasts within pseudotachylyte are elongate polycrystalline quartz clasts with round margins. The percentage of entrained clasts increases near the locally irregular pseudotachylyte and host mylonite margin. Host quartzofeldspathic mylonite is entrained in and cross-cut by pseudotachylyte. Continuous bands of host mylonite

entrained and contained within the pseudotachylyte differs in texture from the encompassing host mylonite surrounding pseudotachylyte. The entrained bands of host mylonite suffer a reduced grain size of all phases and a higher density of intragrain fractures in both plagioclase and potassium feldspar porphyroclasts.

In sample 3-5B, the C-folia-parallel pseudotachylyte vein is composed of two distinct extinction textures in cross-polarized light. A 100 μm -wide margin with no sweeping extinction of biotite separates the two pseudotachylyte textures. In the more prevalent texture there is more biotite, and the amount of biotite increases with distance from the less prevalent pseudotachylyte texture. Light microscopy of clasts within both samples of the pseudotachylyte confirms the elongation of polycrystalline quartz clasts with respect to the C-fabric.

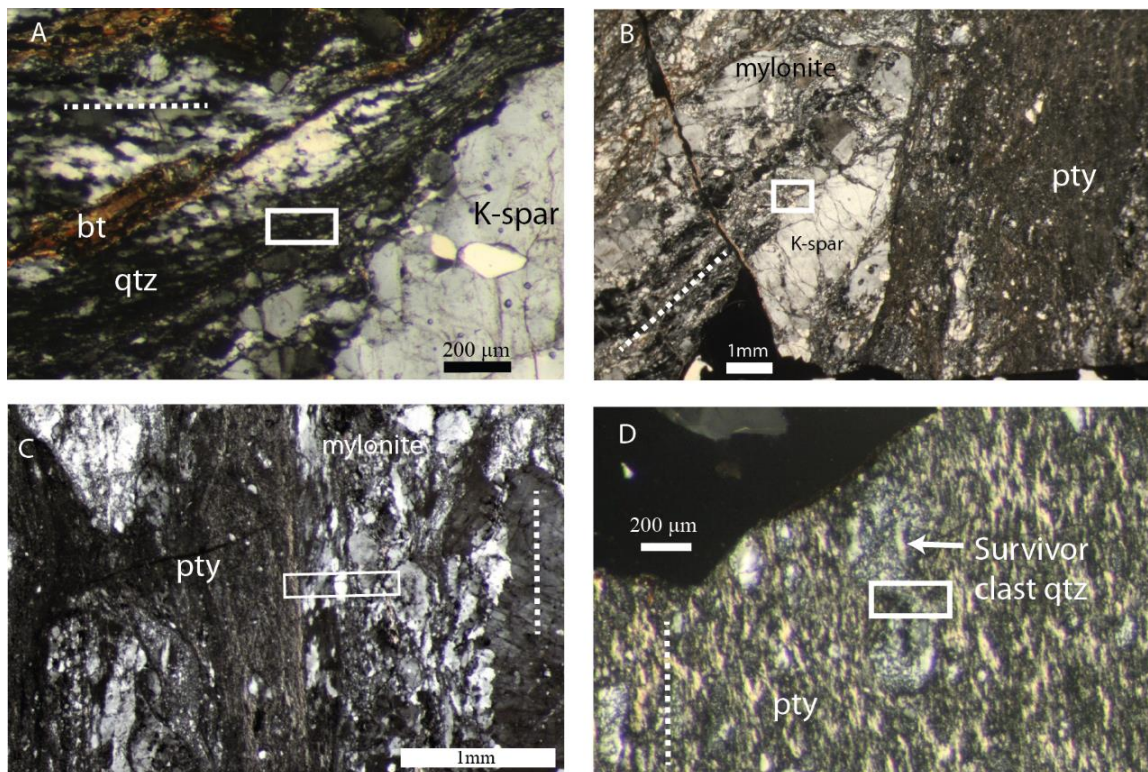


Figure 4: Photomicrographs in cross polarized light of samples A) 08-02, B) 2-7-1, C) 3-5B, and D) an entrained survivor clast in 3-5B. Foliation is marked by dashed white lines and white rectangles indicate areas of EBSD data collection. A) Control mylonite with a quartz grain shape and size fabric ‘pinched’ around a feldspar porphyroclasts. Biotite is also present and marks the S-C fabric of the anastomosing mylonite. B and C) Feldspars retain relict perthite and are brittle porphyroclasts in the greenschist to amphibolite grade host mylonite. Pseudotachylyte veins cross cut the host mylonite, and entrain mylonite. D) Microcrystalline biotite encompasses survivor clasts entrained in the pseudotachylyte and is evidenced by sweeping extinction in cross polarized light.

4.3 EBSD

4.3.1 Microstructures in control mylonite, 0.3 μm step size

The EBSD phase map is composed of dominantly quartz, K-feldspar, and plagioclase, with minor amounts of biotite and allanite (Figure 5). Quartz is most abundant in the map, with larger elongate grains ($>15 \mu\text{m}$ diameter) forming a shape fabric oriented subparallel to the long orientation of the map. The quartz shape fabric is obliquely cut by upper right to lower left oriented linear domains of fine-grained ($<10 \mu\text{m}$ diameter) plagioclase, K-feldspar, and quartz aggregates. In the quartz-rich domain, coarser and elongate grains of quartz have both irregular and straight grain boundaries with local development of small-scale bulging grain boundaries. These coarser quartz grains ($>15 \mu\text{m}$ diameter) display both sinuous and straight subgrain boundaries, and rarely, the subgrains intersect to form four-subgrain junctions. The elongate, coarser quartz grains have fine-grained quartz (2-10 μm diameter) in their interstitial spaces, and the small grains tend to be subequant and somewhat rounded in shape. The subgrain size in the coarse-grained quartz is similar to the size of the largest grains of fine-grained quartz ($\sim 10 \mu\text{m}$ diameter). However, the fine-grained quartz generally lacks subgrains, but where present, the subgrain boundaries are straight. Where there are networks of fine-grained quartz, 4-grain junctions are common. Quartz grain size is finest in the linear zones of polyphase aggregates that cut

across the shape fabric of the coarse-grained quartz, and these fine grains also form 4-grain junctions. All quartz grain size characteristics are shown in Table 2.

The average intragrain misorientation and local misorientation EBSD maps show that there is more lattice distortion in coarse-grained quartz relative to fine-grained quartz, and that the lattice distortion is concentrated along low-angle boundaries (Figure 5, Appendix A). In the average intragrain misorientation map, the blue color of the fine-grained quartz indicates that there is very little lattice distortion within these grains, and the juxtaposition of the blue grains with the other colored grains shows that the blue grain boundaries are convex outward towards grains with higher amounts of lattice distortion (Figure 5). In the local misorientation map, the coarser-grained quartz has more misorientations relative to the fine-grained quartz, where the misorientations are concentrated along both subgrain boundaries ($>2^\circ$ misorientation) and other low-angle boundaries ($<2^\circ$ misorientation) (Appendix A).

Quartz grain orientations in the control mylonite define a strong lattice preferred orientation (LPO), with coarse- and fine-grained fractions contributing to different parts of the LPO (Figure 5). All quartz grains define an elongate cluster of *c*-axes (plotted as poles to [0001]) oriented $\sim 30^\circ$ counterclockwise from the pole to foliation, but the elongate cluster does not extend to the primitive circle. The *c*-axes of coarser quartz grains ($>10\ \mu\text{m}$ diameter) plot completely within the densest part of the elongate cluster. In contrast, the *c*-axes of fine-grained quartz ($<10\ \mu\text{m}$ diameter) plot within the elongate cluster and as scattered points across the pole figure.

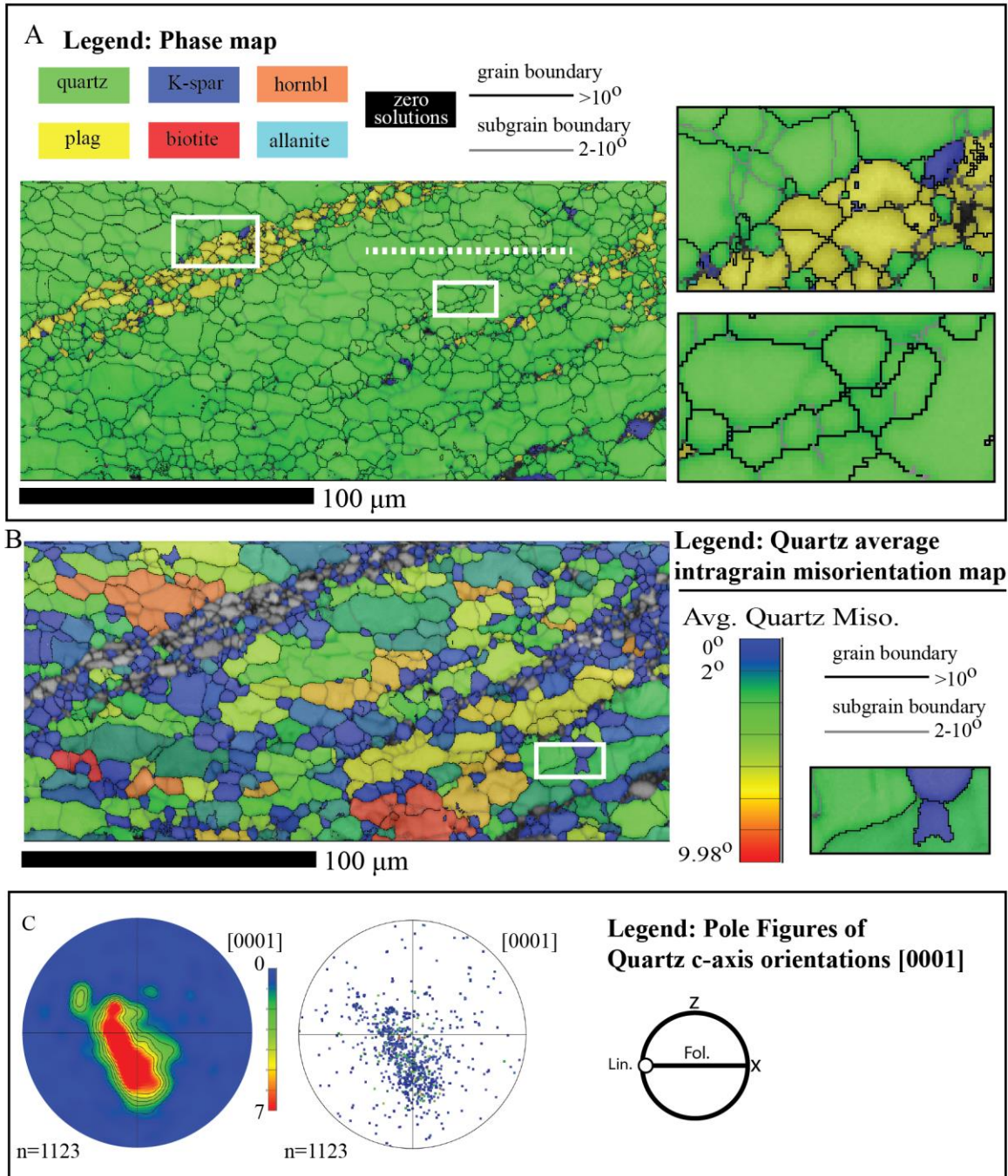


Figure 5: EBSD maps of thin section study area acquired in sample 08-02 with a 0.3 μm step size. Foliation is marked by dashed white line. A) EBSD phase map layered on a band contrast map. The map shows an abundance of quartz cross cut by fine grained ($<10\ \mu\text{m}$ in diameter) plagioclase, K-feldspar, and quartz mixtures with 4 grain junctions and sub-grains displayed in insets. B) EBSD quartz average intragrain misorientation map layered on a band contrast map. The map shows low strain grains in blue and higher strain grains in warmer colors. Inset map highlights a small lobate grain protruding into a grain of higher average intragrain misorientation. C) Pole figures display a point per grain subset of all quartz c-axes [0001] in lower hemisphere stereographic projections with reference to the observed foliation: one is contoured with a halfwidth of 10° and a max m.u.d of 7, while another is not contoured, but each grain of quartz is colored, corresponding to its average intragrain misorientation in map 5b.

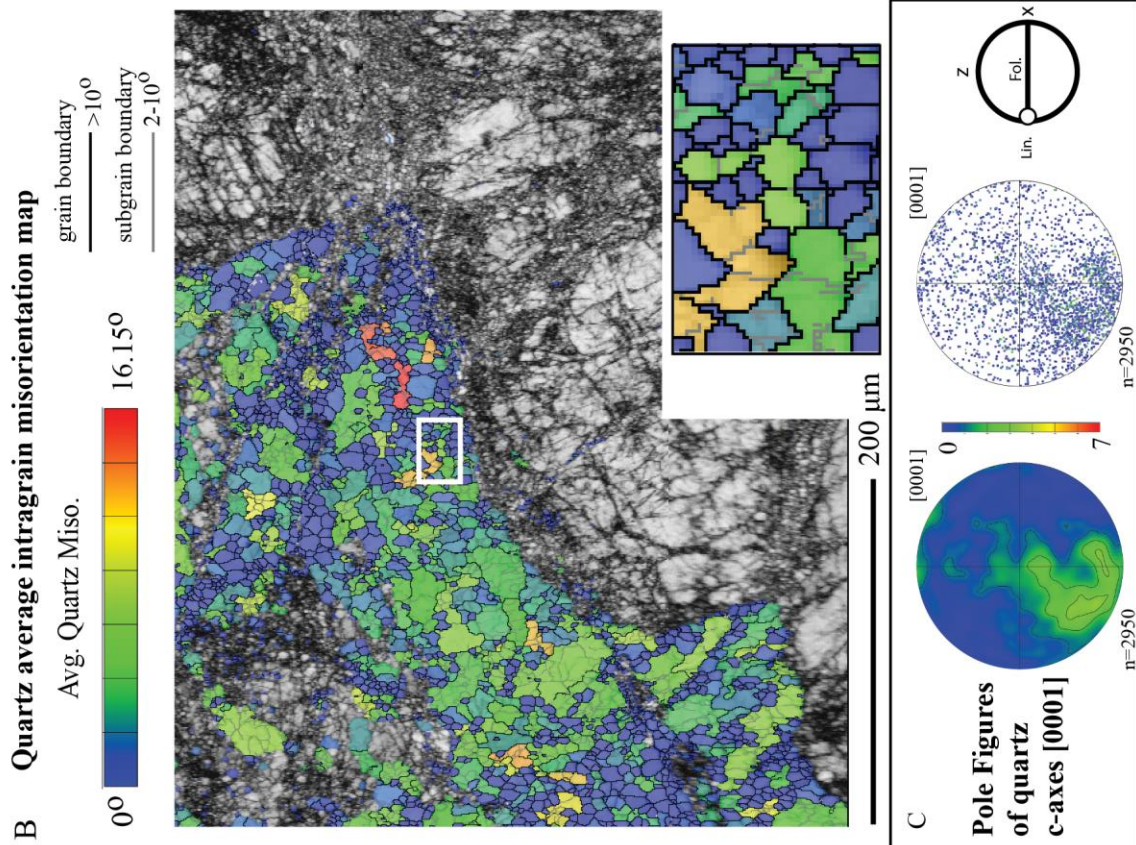
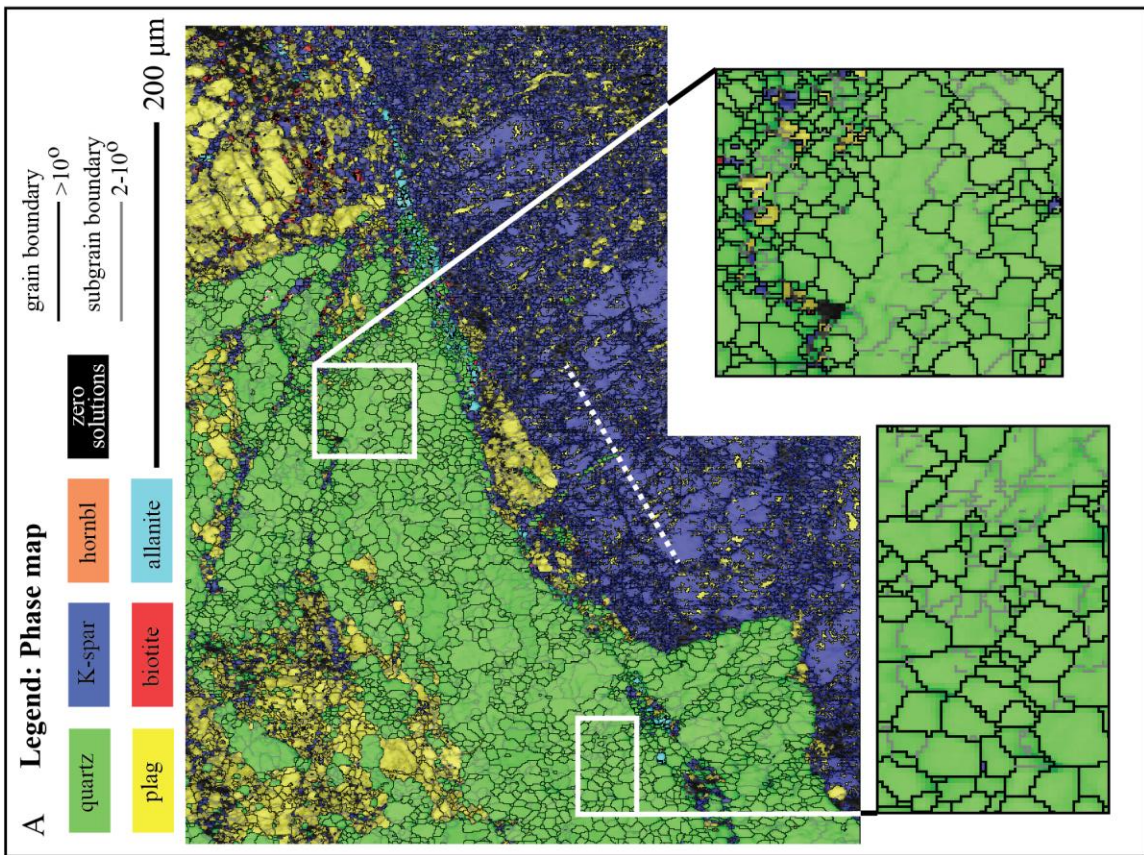


Figure 6: EBSD maps of thin section study area in sample 2-7-1 acquired with a 0.75 μm step size. Foliation is marked with a dashed white line. A) EBSD phase map layered on a band contrast map. The map shows the interaction between a larger K-feldspar porphyroblast, smaller plagioclase porphyroblast and domain of quartz. Insets highlight bulging relationships between elongate host grains and interstitial recrystallized grains, along with the subequant polygonal shape of recrystallized quartz aggregates that are arranged with 4 grain junctions. B) EBSD quartz average intragrain misorientation map layered on a band contrast map. The map shows low strain grains in blue and higher strain grains in warmer colors. Inset targets small lobate grains protruding into grains of higher misorientation. C) Lower hemisphere stereographic projections display an identical data set; a point per grain subset of all quartz c-axes [0001] in reference to the observed foliation: one is contoured with a halfwidth of 10° and a max m.u.d of 7 and another is not contoured but each grain of quartz is colored, corresponding to its average intragrain misorientation in 6b.

4.3.2 *Microstructures within host mylonites to pseudotachylytes, 0.75 μm step size*

The EBSD maps of host mylonite reveal crystal-plastic deformation of quartz. The coarser-grained quartz ($>15 \mu\text{m}$ diameter) is commonly elongate with inequigranular, amoeboid grain boundaries, whereas the fine-grained quartz ($<10 \mu\text{m}$ diameter) is either rounded and equant, or slightly elongate with straight grain boundaries (Figure 6). Subgrains are well-developed within the coarser-grained quartz, and nearly absent in the fine-grained quartz. Where present, most subgrain boundaries are curved or irregular, though there are rare junctions where four diamond-shaped subgrains meet. The average intragrain misorientation map (Figure 6) shows that there is more lattice distortion in coarse-grained quartz relative to fine-grained quartz. The local misorientation map (Appendix A) shows that lattice distortion accumulates along subgrain walls and other low-angle boundaries within the coarser grains, and that neither diffuse lattice distortion or low-angle boundaries are common in fine-grained quartz.

The EBSD maps of host mylonite show that both feldspars are brittlely fractured, and that there is local development of crystal plastic deformation in K-feldspar (Figure 6). The K-feldspar porphyroblast is dissected by discrete, intragrain fractures, but it also shows local development of serrate grain boundaries along its rim and zones of extremely fine

grains confined to intragrain fractures. The fine grains within the fractures are not angular, nor is there significant matrix developed around them (see band contrast image in Figure 6). Similarly, the plagioclase porphyroclast has intragrain fractures, and they are filled with mixtures of K-feldspar and biotite (Figure 6). Linear networks of fine-grained K-feldspar, biotite, and plagioclase extend from a few plagioclase porphyroclast intragrain fractures and define a K-feldspar porphyroclast tail. These linear networks cut across the grain shape fabric of the quartz. All quartz grain size characteristics are shown in Table 2.

The quartz grain orientations define a weak to moderate LPO pattern. Quartz *c*-axes form a weak cross girdle rotated 30° from the pole to foliation (Figure 6). Most coarse-grained quartz orientations plot in the densest part of the cross girdle fabric, but the *c*-axes of fine-grained quartz (diameter <10 μm) plot with a greater dispersion around the cross girdle. Coarser grains of quartz (diameter >10 μm) that are surrounded by mixtures of other minerals also have *c*-axes that plot with a greater dispersion around the cross girdle.

The EBSD phase map of the contact between a pseudotachylyte vein and its compositionally layered host mylonite reveal extensive crystal-plastic deformation of quartz in both rock types (Figure 7). The host mylonite is very strongly compositionally layered, with a quartz-rich domain in contact with the pseudotachylyte vein. The coarsest quartz grains in this domain are very elongate with high aspect ratios, and have grain boundaries that are highly irregular and lobate. These coarser grains have extensive subgrain development and are surrounded by an interconnected network of fine quartz grains that are also elongate, but with straighter grain boundaries relative to the coarser grains. Four-grain junctions are common within the fine-grained quartz. The host mylonite quartz grains directly in contact with the pseudotachylyte form a distinct ~5 μm thick

margin of ultrafine-grained quartz separating host mylonite and pseudotachylyte. The pseudotachylyte vein is parallel to the host mylonite foliation, and contains quartz-rich survivor clasts that occur as coarser, single grains and as polycrystalline clasts. Survivor clasts of plagioclase and K-feldspar, biotite, and allanite are less common. All quartz-rich survivor clasts within the pseudotachylyte are elongate parallel to mylonitic foliation. Quartz grains entrained in the pseudotachylyte have an average aspect ratio of 1.9. All quartz grain size characteristics are shown in Table 2.

The EBSD phase map also shows brittle deformation of plagioclase and some relict exsolution and myrmekite textures preserved within coarser clasts of feldspar (Figure 7). The layer of plagioclase feldspar is intensely fractured, and fine-grained K-feldspar is common within the fractures, though some fractures are filled with fine-grained mixtures of K-feldspar, quartz, biotite, and allanite. The margin between the fractured plagioclase layer and crystal-plastically deformed quartz layer is diffuse in that it is marked by a zone where fine-grained plagioclase, quartz and K-feldspar are mixed. In the center of the fractured plagioclase layer, relict exsolution textures are preserved within coarser clasts of plagioclase, and are evident as intragrain blebs of K-feldspar. Similarly, relict myrmekite texture is preserved as isolated intragrain blebs of quartz within coarser clasts of plagioclase.

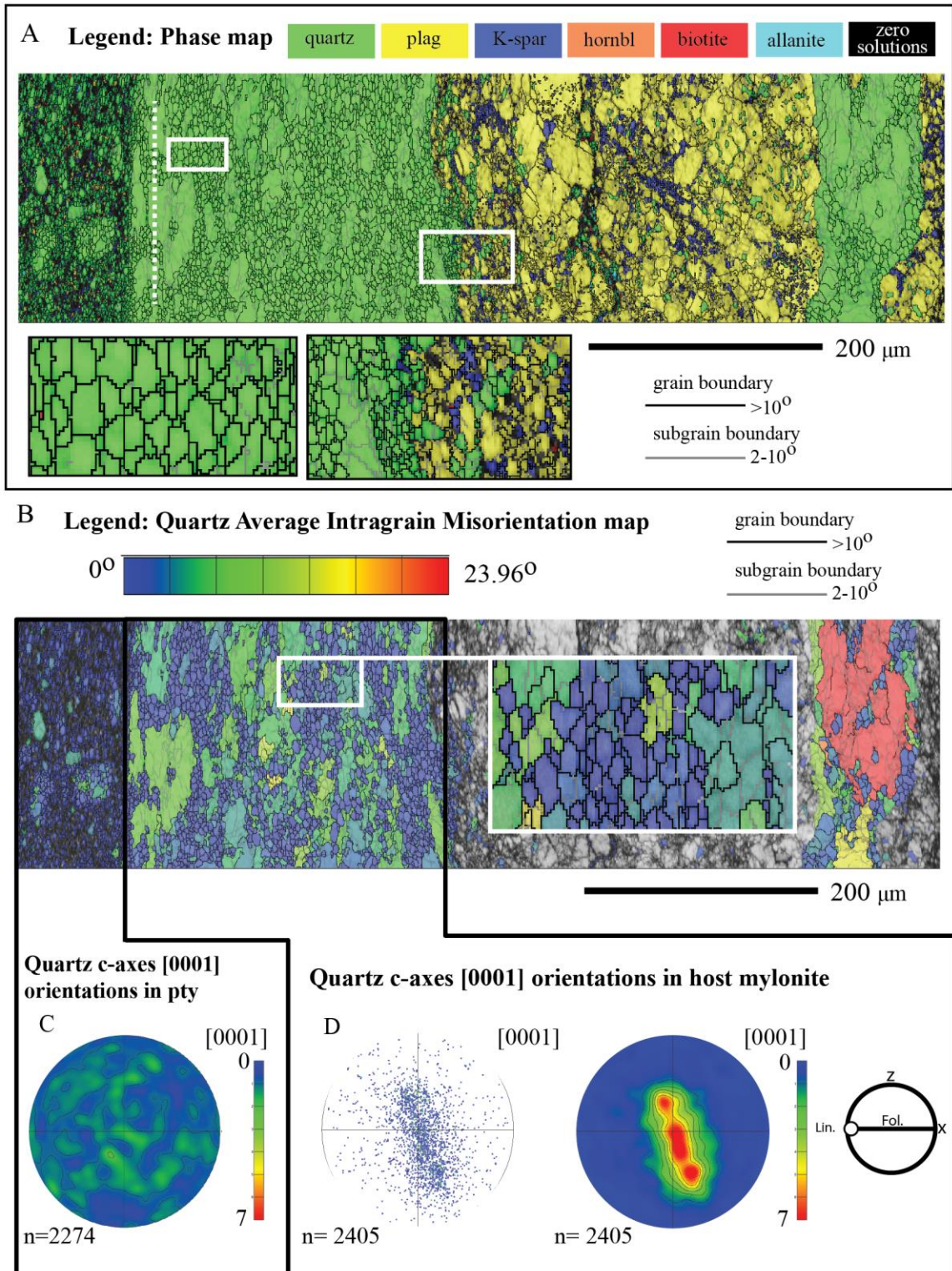


Figure 7: EBSD maps of thin section study area in sample 3-5B acquired with a 0.75 μm step size. Foliation is marked with a white dashed line. A) EBSD phase map layered on a band contrast map. The map shows the fringes of a pseudotachylyte vein located on the left that is adjacent to a domain quartz, as well as a plagioclase feldspar porphyroclast. Insets highlight 4-grain and sub-grain junctions, with straight grain boundaries, as well as phase mixing along the plagioclase porphyroclasts. B) EBSD quartz average intragrain misorientation map layered on a band contrast map. The map shows low

strain grains in blue and higher strain grains in warmer colors. Inset highlights small grains protruding into grains of higher misorientation, along with the development of straight grain boundaries in fine recrystallized grains. Pole figures are lower hemisphere stereographic projections displaying a point per grain subset of all the quartz *c*-axes [0001] to which they are bounded in reference to the observed foliation: C) includes all grains located in the pseudotachylyte (pty) and is contoured with a halfwidth of 10° and a max m.u.d of 7. D) consists of two pole figures displaying identical datasets of host mylonite where one is contoured identically to 7c, and another is not contoured but each grain of quartz is colored, corresponding to its average intragrain misorientation in 7b.

The EBSD misorientation maps of host mylonite and pseudotachylyte show that the larger, elongate quartz grains have more lattice distortion relative to the fine-grained quartz (Figure 7), and that the misorientations that contribute to the lattice distortion are concentrated along low-angle boundaries within the coarser grains (Appendix A). In the host mylonite, the proportion of dark blue grains is large relative to the other colors, indicating a high recrystallized fraction (Figure 7). These dark blue grains tend to be fine grained (<10 μm in diameter), and devoid of subgrains. The small dark blue recrystallized grains are elongate, with many forming diamond shapes; four-grain junctions are common. The larger, elongate grains have higher misorientation content, and the misorientations are organized along subgrain walls (Appendix A). In these grains, subgrain walls are oriented at small angles to foliation so that the subgrains appear elongate in shape. In the pseudotachylyte, survivor clasts are dominated by fine-grained quartz with few subgrains. Like the fine-grained quartz in the host mylonite, the fine-grained quartz in survivor clasts also show four-grain junctions.

The host mylonite quartz *c*-axis orientations define a strong LPO, but subsets of finer-grained quartz in the host mylonite and in adjacent pseudotachylyte both have a randomized LPO pattern (Figure 7). The *c*-axes of host mylonite quartz grains form a half girdle where the long dimension of the girdle is oriented ~20° counterclockwise from the pole to foliation. However, the *c*-axis orientations coarser-grained quartz are tightly

clustered within this half girdle compared to the *c*-axis orientations of recrystallized grains. Similarly, pseudotachylyte survivor clast quartz grains have random orientations of *c*-axes.

4.3.3 Microstructures of survivor clasts, 0.3 μm step size

EBSD maps of survivor clasts and pseudotachylyte (Figure 8) show a predominance of fine-grained, polycrystalline quartz clasts within a matrix that varies from glassy to microlite-rich based on EBSD indexing of optically observed pseudotachylyte (Figure 8). Most survivor clasts are elongate parallel to foliation and are rimmed by a layer of extremely fine-grained quartz that is in contact with the pseudotachylyte glass. The polycrystalline survivor clasts are almost uniformly fine-grained (<10 μm in diameter), with a high proportion of fine grains (up to 90%) relative to relict coarser grains. The rare coarser grains are irregular in shape, have subgrain development, and local bulging grain boundaries (Figure 8). The fine grains have few subgrains, and vary from being rounded and equant in shape to slightly elongate and diamond-shaped. Four-grain junctions are common in the fine-grained quartz of the polycrystalline survivor clasts; we also observe X-shaped junctions between quartz grains and subgrains (Figure 8). Though the polycrystalline survivor clasts are nearly all quartz, there are rare grains of interstitial and extremely fine-grained biotite, and at least one place where a somewhat linear network of mixed grains of K-feldspar, plagioclase, biotite, and allanite cut through a polycrystalline clast (Figure 8). All quartz grain size characteristics are in Table 2.

Legend: Phase map

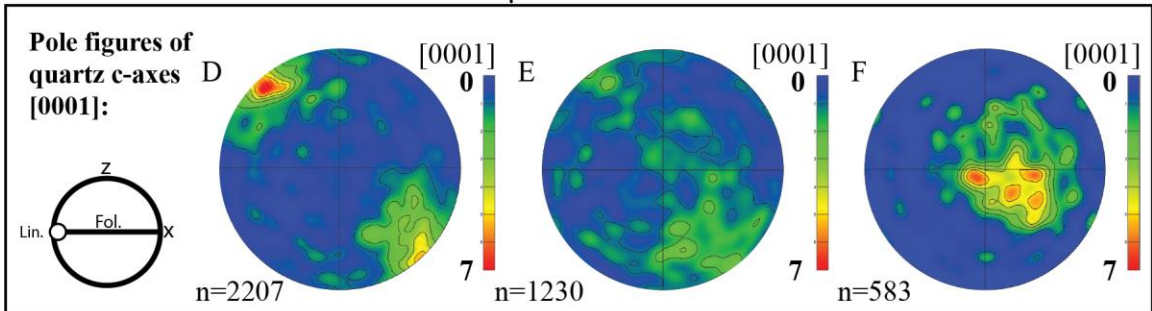
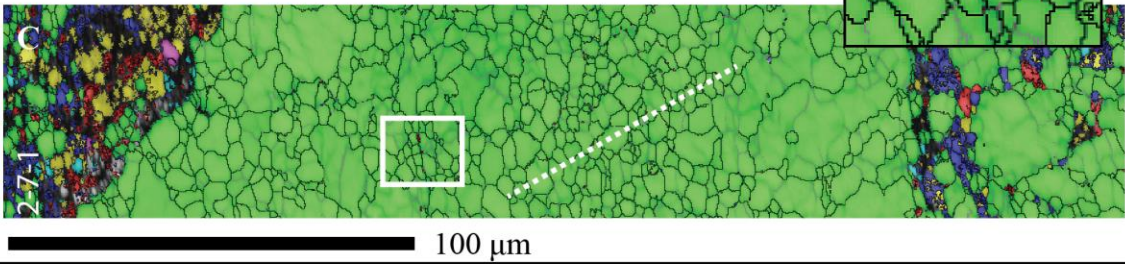
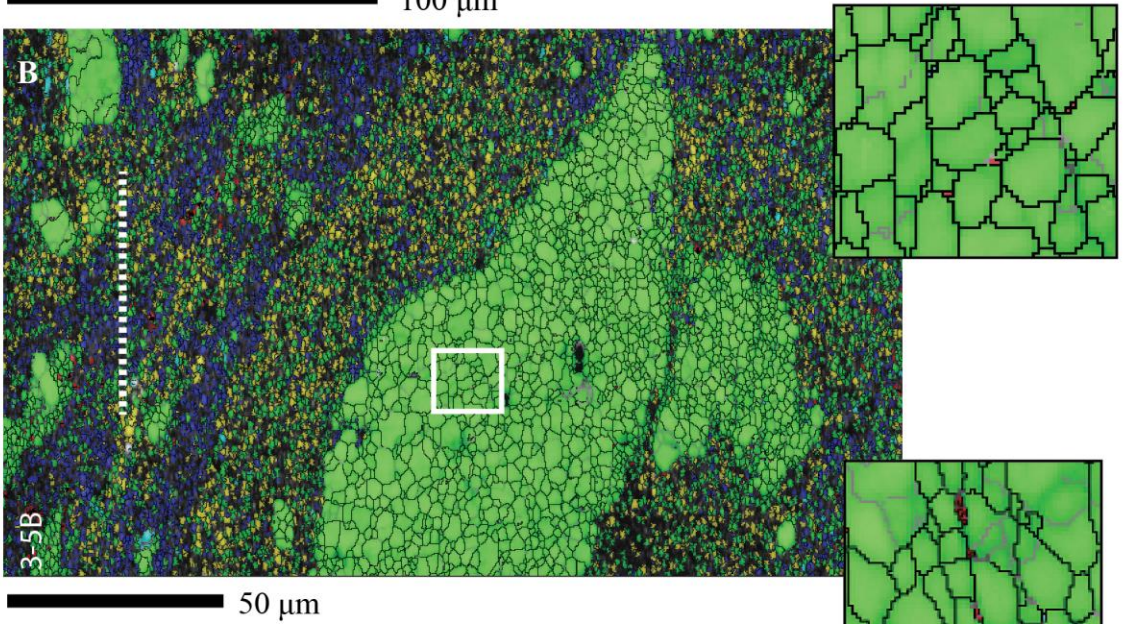
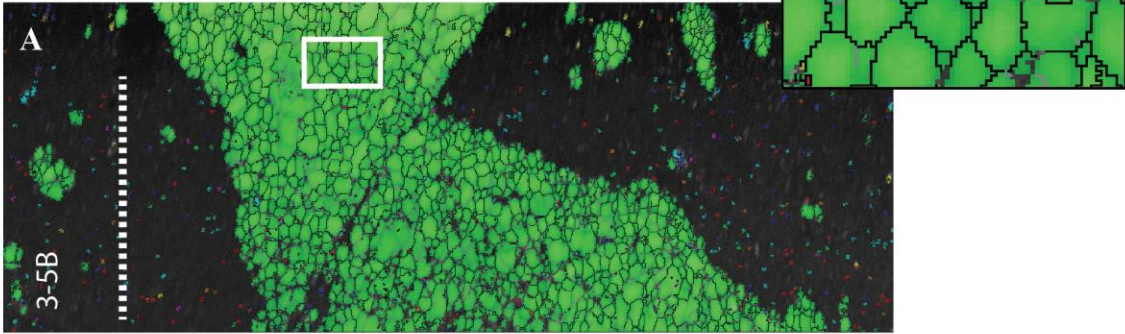
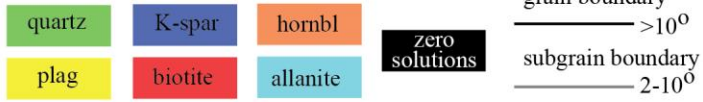


Figure 8: EBSD phase maps of thin section study areas acquired in samples 2-7-1 and 3-5B with a 0.3 μm step size. Foliation for each sample is marked with a dashed white line. A) EBSD phase map from sample 3-5B layered on a band contrast map. The map displays a discrete right lateral fracture through a survivor clast of polycrystalline quartz entrained in pseudotachylyte. B) EBSD phase map from sample 3-5B layered on a band contrast map. The map displays a sigmoid shaped fine grained polycrystalline quartz clast entrained in pseudotachylyte. C) EBSD phase map from sample 2-7-1 layered on a band contrast map. The white rectangles indicate the location of insets located to the top right of each respective map highlighting the prevalence of 4 grain junctions, sliding surfaces, and interstitial biotite grains in each map. Pole figures display a point per grain subset of quartz c -axes [0001] from grains located in the dominant survivor clast for their respective map: A and D; B and E; C and F. Each is contoured with a halfwidth of 10° and a max m.u.d of 7.

Polycrystalline survivor clast quartz c -axis orientations define a moderate to strong LPO (Figure 8). In the pole figure corresponding to Figure 8a, the quartz c -axis orientations define a strong LPO where two maxima are oriented $\sim 45^\circ$ counterclockwise from the pole to foliation. The pole figure corresponding to Figure 8b shows a weaker LPO with similar geometry to the previous one, but with the peripheral maxima starting to randomize. The pole figure corresponding to Figure 8c is moderate in strength and distinct from the other two in that the c -axes define a somewhat circular maximum that is slightly offset from the center of the pole figure and diffuse at its edges.

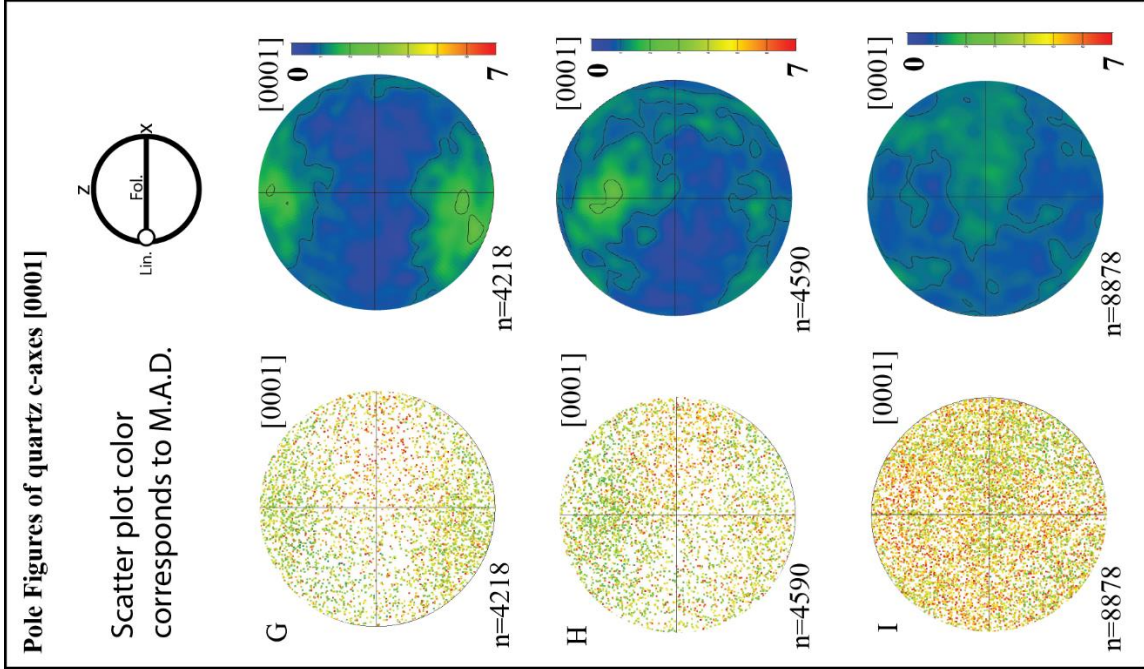
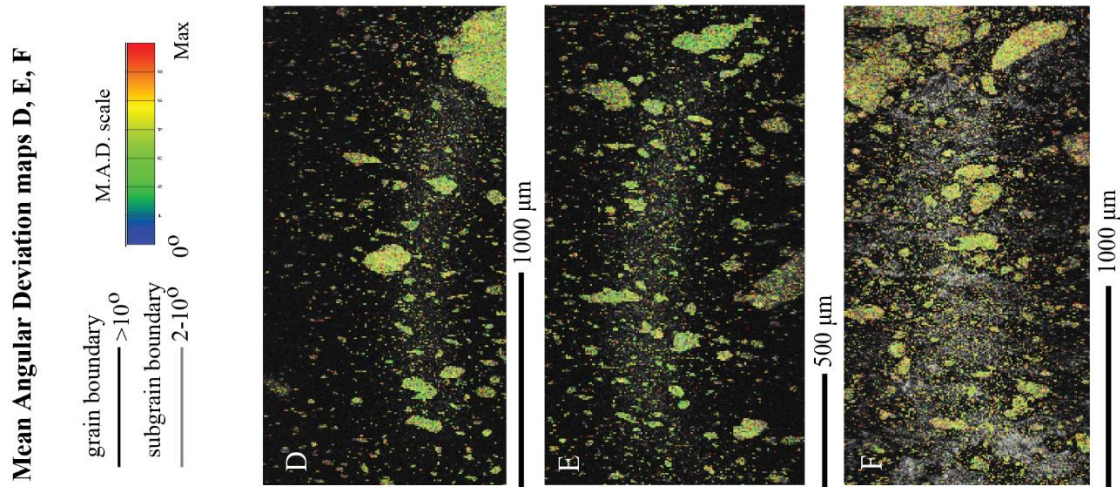
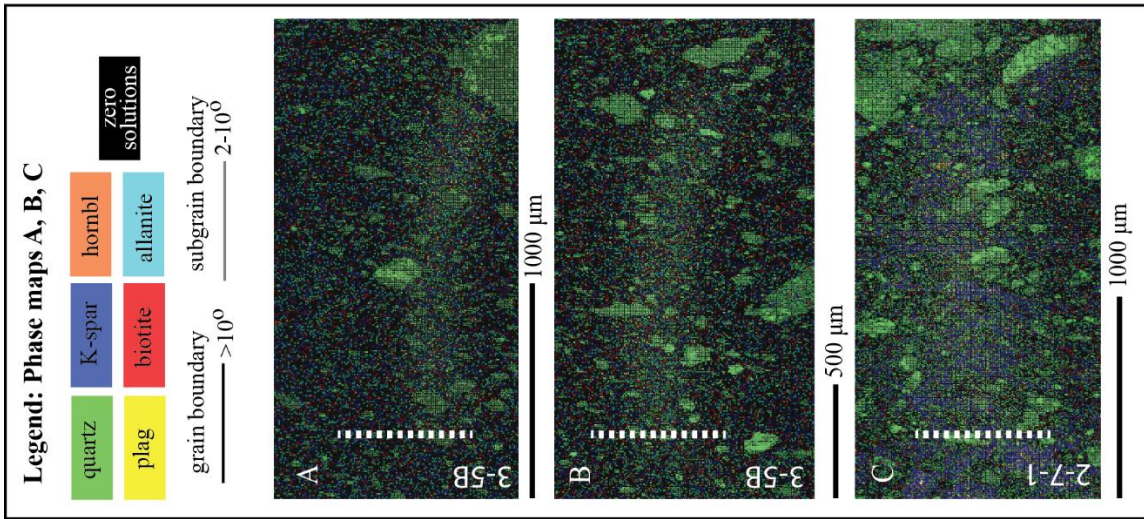


Figure 9: EBSD data sets collected from samples 3-5B and 2-7-1 of pseudotachylyte. Map areas were chosen to be representative of the entire pseudotachylyte vein in each sample and were collected with a 7 μm step size. Foliation for each vein is marked with a white dashed line. Maps A, B, and C are phase maps showing the dominance of survivor quartz while D, E and F display quartz M.A.D. values for the same dataset. Quartz M.A.D. values were filtered so that only the best 50% of quartz grains are colored, and plotted in pole figures (max M.A.D values were set to 0.61, 0.60, 0.67 respectively). G, H, and I) Pole figures are lower hemisphere stereographic projections in reference to each samples' foliation and display point per grain datasets corresponding to maps D, E, and F plotted in both scatter and contour plots with a halfwidth of 10° and a max m.u.d. pinned at 7.

4.4 Piezometry

Piezometry calculations based on recrystallized grain diameters show moderate to high differential stress estimates for all samples. The differential stress estimates are lowest in the control mylonite (~ 100 MPa), and higher in the mylonites that are host to pseudotachylyte veins ($\sim 120 - 160$ MPa). The differential stress estimates derived from polycrystalline survivor clasts are the highest of all, ranging from ~ 260 MPa to upwards of ~ 400 MPa. All average grain diameters and the corresponding differential stress calculations and associated errors are shown in Table 2. However, the average grain diameters in two of the pseudotachylyte survivor clasts are lower than the estimated range of grain sizes for which the piezometer may be applied (Stipp and Tullis, 2003).

Texture	Sample	aspect ratio		grain diameter		# of grains	Piezometry	Fine grain quartz		Recrystallized quartz	
		avg (μm)	max (μm)	recrystallized (μm)	max (μm)			Differential Stress (MPa)	(d < 10)	(avg miso < 2)	% out of total quartz
Control mylonite	08_02	1.6	7.3	4.5	26.7	n=726	104 (+16/-12)	42	40.5		
Host mylonite	2_7_1	1.7	5.7	4.1	36	n=2481	122 (+14/-13)	42	47.8		
Host mylonite	3_5B	2.1	8.6	3.5	74.4	n=2263	160 (+15/-16)	70	57.4		
Survivor clasts	3_5B	1.5	4.6	2.6	17.3	n=1978	263 (+32/-23)	90	66.1		
Survivor clasts	3_5B	1.7	6.3	1.8	9.8	n=1361	483* (+77/-76)	100	86.2		
Survivor clasts	2_7_1	1.7	7.19	2	30.4	n=679	403* (+30/-30)	59.1	43.4		

* calculated from a grain size not within the calibrated range for the Stipp and Tullis (2003) piezometers

Table 2: Grain size data consolidation for each high resolution EBSD dataset. Errors are derived from standard error in grain size propagated through the published error on the Stipp and Tullis (2003) piezometer for bulging recrystallization in quartz.

Chapter 5: Discussion

5.1 Deformation of Quartz and Feldspars

All three samples have quartz microstructures that are consistent with dynamic recrystallization during dislocation creep where deformation was initially accommodated by subgrain rotation recrystallization (SGR), and later by low-temperature bulging recrystallization (BLG). The prevalence of subgrains in the coarser-grained quartz and the similar size of the subgrains and some adjacent recrystallized grains points to an origin by SGR. However, the sinuous and lobate grain boundaries of the coarser relict grains indicates some subsequent modification. Though the lobate shapes superficially resemble those associated with high-temperature grain boundary migration (GBM), the size of the lobes (a few μm in diameter) is more consistent with the small scale bulges associated with the BLG mechanism. This is supported by the smaller size of the rounded and equant recrystallized grains (neoblasts from BLG) relative to the larger subgrain size in quartz 'porphyroclasts'. The overprinting of SGR microstructures by BLG microstructures suggests that dislocation climb became increasingly difficult during progressive deformation, and that dislocation glide became more dominant; this could have been achieved by down-temperature deformation and/or with increasing strain rate during deformation, and may also be influenced by water content (e.g., Hirth and Tullis, 1992; Stipp et al., 2002; Stipp et al., 2010; Law, 2014).

All three samples indicate brittle deformation of plagioclase and K-feldspar, with very limited crystal plastic deformation and recrystallization. The local development of serrate grain boundaries and extremely small, subrounded neoblasts in zones along

intragrain K-feldspar fractures indicates limited bulging recrystallization along fractures and porphyroclast rims (Figure 6). Though most feldspar deformation is brittle in nature, there is little offset and limited grain size reduction along fractures (Figure 6 and Figure 7). The fine-grained phase mixtures observed along fractures may instead be explained by small amounts of offset and grain rotation along fractures that cut fine-grained, relict exsolution and myrmekite textures in the feldspar. The presence of biotite along many fractures (Figure 6 and Figure 7) indicates that fluid flow along fractures may have assisted in the nucleation and growth of minerals, further enhancing phase mixing. The association of phase mixtures with feldspar fractures and feldspar porphyroclast tails indicates that both brittle deformation and very limited crystal plastic deformation promoted the development of phase mixtures. Of particular significance is that the linear zones of phase mixtures develop largely after quartz grain shape fabric development, based on the cross-cutting relationships (Figure 5 and Figure 6).

5.2 Quartz LPO Evolution and Deformation Mechanisms

The control mylonite and the host mylonites show quartz LPO development consistent with well-known slip systems, but small grains with low values of intragrain misorientation within the plots show a trend towards randomization. The control mylonite has LPO development consistent with the operation of rhomb $\langle a \rangle$ and prism $\langle a \rangle$ slip systems, but the grains scattered away from the maximum are blue and correlate with low values of average intragrain misorientation, which are dominantly small recrystallized grains (scatter plot in Figure 5). The host mylonite samples show two LPO variations: a pattern consistent with operation of basal $\langle a \rangle$, rhomb $\langle a \rangle$, and prism $\langle a \rangle$ slip (Figure 6), and another LPO pattern consistent with operation of rhomb $\langle a \rangle$ and prism $\langle a \rangle$ slip (Figure

7). Similarly, in both of these host mylonite samples, the grains that are dispersed from the maxima are small with low average intragrain misorientation (scatter plots in Figure 6 and Figure 7).

The dispersion of small, low-strain quartz grains away from the densest parts of the maxima is produced by small amounts of progressive misorientation through recrystallization during dislocation creep, and then by larger amounts of misorientation through grain boundary sliding (GBS) associated with diffusion creep. In naturally deformed quartz, both BLG and SGR have been shown to produce progressively misoriented recrystallized grains with respect to parent grains, resulting in a similar, but more diffuse LPO pattern in recrystallized grains (e.g., Bestmann and Prior, 2003; Mariani et al., 2009; Halfpenny et al., 2012). However, some recrystallized grain orientations lie outside of the $\sim 10^\circ$ cone around parent grains, and GBS has been invoked by many researchers to explain this observation (e.g., Zhang et al., 1994; Halfpenny et al., 2006; Skemer and Karato, 2008; Rahl and Skemer, 2016). In our control and host mylonite samples, the proximal locations of recrystallized grains around parent grains is consistent with misorientation through SGR and BLG, but the more distal locations of small, low strain grains with respect to parent grains is more consistent with randomization due to GBS (Figures 5, 6, and 7).

The onset of GBS in our samples is supported by the presence of microstructures that are indicative of grain size sensitivity and associated GBS. Typical microstructural traits of grains that deform by GBS include 1) fine grain sizes ($d < 10 \mu\text{m}$), 2) equant, polygonal shapes, 3) strain-free grains, 4) smaller neoblasts relative to subgrain size, 5) alignment of straight edges of grains to produce sliding surfaces, and 6) four-grain

junctions indicative of neighbor switching (e.g., Ashby and Verrall, 1973; Mohamed and Langdon, 1976; White, 1979; Halfpenny et al., 2006; Halfpenny et al., 2012). The recrystallized grains in our control and host mylonites have all of these traits in addition to some LPO randomization, indicating that the onset of GBS occurred in rocks prior to pseudotachylyte formation.

Our data indicate that limited GBS continued in survivor clasts during pseudotachylyte formation, and that the randomization of survivor clast LPO patterns was instead achieved by rigid body rotation of clasts within a weaker, melt-rich matrix. The four-grain junctions and aligned sliding surfaces of grains in the polycrystalline survivor clasts indicate GBS, yet there is LPO present in the individual polycrystalline clasts (Figure 8). These seemingly contradictory observations do not preclude the operation of GBS, as relict LPOs can be slow or difficult to randomize even after large amounts of strain (e.g., Mainprice, 2009). This effect is enhanced where recrystallized fractions are low (< 50%), leading researchers to infer an inverse relationship between LPO strength and recrystallized fraction (e.g., Rahl and Skemer, 2016). At first glance, our data seem contrary to this finding; there is no systematic weakening of LPO in polycrystalline survivor clasts with increasing recrystallized fraction. However, when we consider multiple quartz survivor clasts (single grain and polycrystalline), the LPO patterns are randomized (Figure 7 and Figure 9). We infer that a minor amount of GBS was accommodated by polycrystalline clasts during pseudotachylyte development preceding quenching because the clasts are elongate, yet they retain LPO and are not appreciably disaggregated within the glassy matrix. The minor amount of disaggregation and rare fractures (Figure 8) suggests that the polycrystalline clasts were more rheologically competent than the melt at the time of

pseudotachylyte generation, and that strain became partitioned into the melt. The flow of melt around survivor clasts could enable rigid body rotation of the survivor clasts and promote randomization of the LPO patterns.

5.3 Rheological Evolution during the Earthquake Cycle

Normal faulting and associated footwall denudation promoted a transition in deformation mechanism, providing an effective means of strain localization that was crucial to subsequent nucleation of pseudotachylyte. The denudation of the South Mountains core complex footwall occurred at progressively cooler temperatures, which promoted a narrowing of the shear zone and the overprinting of higher-temperature dynamic recrystallization microstructures by lower-temperature microstructures (e.g., Reynolds, 1985; Reynolds et al., 1986; Fitzgerald et al., 1993; Greenberg, 2010; Annis, 2012). Grain size reduction during down-temperature dynamic recrystallization can induce a transition to grain size sensitive creep, which is regarded as an extremely effective mechanism of microstructural weakening and strain localization due to the decrease in effective viscosity and/or increase in strain rate associated with crossing the field boundary (e.g., Burgmann and Dresen, 2008; Killian et al., 2011; Platt and Behr, 2011; Czaplinska et al., 2015). The transition from SGR to BLG is consistent with an increase in strain rate (e.g., Hirth and Tullis, 1992; Stipp et al., 2002; Law, 2014), and this rate may have been further increased at the field boundary by the onset of GBS in BLG-nucleated neoblasts. The networks of neoblasts deforming by GBS were likely lower in effective viscosity relative to the rest of the rock due to the weaker nature of the nearly strain-free neoblasts relative to the strain-hardened coarser grains. Strain was therefore effectively localized

within the neoblasts deforming by GBS due to the high strain rate and low effective viscosity, providing a weak substrate in which pseudotachylyte could develop.

Phase mixing is an additional process that promotes sustained strain localization within fine-grained parts of the mylonite. However, the cross-cutting relationships between the recrystallized quartz fabric and the linear zones of mixed phases demonstrate that phase mixing occurs largely after the transition in quartz deformation mechanism. We note that many linear zones of polyphase mixtures extend from the margins of feldspar porphyroclasts, implying that fracturing of feldspar played a role in the initiation of phase mixing. The fine-grained myrmekite and exsolution textures exposed by the fractures were likely entrained into the polyphase mixtures, and aided by fluid flow that promoted additional growth of fine-grained minerals. The importance of phase mixing in keeping strain localized during grain size sensitive deformation is emphasized in a variety of rock types (e.g., Gueydan et al., 2001; Linckens et al., 2011; Platt et al., 2014; Czaplinska et al., 2015; Linckens et al., 2015; Platt, 2015), and we emphasize it here as a contributing factor to strain localization, but the lack of polyphase survivor clasts in pseudotachylyte indicates that the dominant strain localization processes relevant to pseudotachylyte development are those at work in the networks of quartz neoblasts.

The networks of neoblasts deforming by GBS were preferentially exploited during pseudotachylyte development. The prevalence of GBS microstructural traits in the quartz polycrystalline survivor clasts indicates a close association between pseudotachylyte development and the zones of GBS. The networks of neoblasts deforming by GBS are developed parallel to mylonitic foliation, and as foliation planes represent zones of weakness (e.g., Montesi, 2013), we regard the weak zones as critical to pseudotachylyte

development. This may also explain the tendency for pseudotachylyte veins to be oriented sub-parallel to host mylonite foliation. If pseudotachylyte in mylonites represents the downward propagation of rupture along brittle Andersonian faults into ductile shear zones (e.g., Sibson, 1980; Price et al., 2012; Rowe and Griffith, 2015), then the nearly co-planar nature of pseudotachylyte and host mylonite foliation in this location may point to a different origin.

The increasing strain rates associated with grain size evolution in the South Mountains footwall presents an intriguing possibility: did the transition to GBS lead to a runaway increase in strain rate that promoted the *in situ* development of foliation-parallel pseudotachylyte during an earthquake? Conventional models of lithospheric strength show a maximum strength of the crust at the BDT (e.g., Sibson, 1983; Burgmann and Dresen, 2008), but compilations of brittle strength measurements indicate that brittle faults are far weaker than the underlying ductile rocks, making it difficult for brittle faults in the seismogenic zone to transfer stress downward into strong ductile crust (Behr and Platt, 2014). Instead, weak faults in the seismogenic zone may be loaded from below by a strong ductile crust. The development of *in situ* pseudotachylyte from runaway increases in strain rate associated with the onset of GBS may be a manifestation of this ‘bottom-up’ model of stress transfer, although we cannot evaluate if stress was transferred to the brittle detachment fault as it is not preserved in the pseudotachylyte localities. However, the differential stresses that we calculate from piezometry are high and consistent with the upper end of the ductile crustal strength measurements compiled by Behr and Platt (2014), indicating the potential for ‘bottom-up’ stress transfer.

In the absence of physical continuity between the brittle detachment fault and the pseudotachylytes of this study, we consider two end-member models: the high stresses in the pseudotachylytes and host mylonites either represent transient states of stress associated with the tip of a downward propagating rupture (traditional model), or that they are indicative of plastic instabilities that lead to *in situ* and coeval pseudotachylyte formation beneath the seismogenic zone (a more contentious model). In the former scenario, the stress accumulations at the tip of a fault beneath the BDT causes short term deformation at high strain rates (Ellis and Stockhert, 2004). These stress ‘blips’ cause large increases in differential stress (> 200 MPa above ambient stress levels) beneath the BDT that decay over the course of decades. In contrast, the latter scenario involves dislocation glide-accommodated plastic instabilities that produce localized heating as a consequence of the mechanical work involved in glide (Fressengeas and Molinari, 1987), which can in turn generate pseudotachylyte (White, 2012). We favor the latter model, though we acknowledge the possibility that a hybrid of these two end members is possible, where accelerated creep within localized zones of GBS leads to upward linkage with brittle faults in the seismogenic zone.

We argue for the coeval development of pseudotachylyte and mylonitic fabric beneath the BDT. In the traditional ‘top-down’ propagation model, a cross-cutting relationship is implied by a high-angle fault that propagates into a low-angle ductile shear zone (Ellis and Stockhert, 2004), but we do not see such orientation relationships in the field. Though we do document high differential stresses and infer high strain rates that are consistent with this model, the difficulty surrounding a weak fault’s ability to transfer stress to a strong ductile crust (Behr and Platt, 2014) argues against this origin for the

pseudotachylyte. Instead, our field and microstructural observations are more consistent with other studies of coeval pseudotachylyte and ductile shear. White (1996; 2012) also documents the importance of a ductile precursor to pseudotachylyte development, as pseudotachylytes are confined to the core of an ultramylonite shear zone where strain is localized. In these studies, the abundance of glide accommodated dislocations and the preponderance of recovery microstructures indicate the dominance of high strain rate deformation (Peierls stress). Our samples show evidence of glide through the development of BLG microstructures, but we see recovery microstructures in the form of recrystallized neoblasts, which would seem to remove the driving force for localized heating. However, the onset of GBS might have accelerated the strain rate fast enough to facilitate an upwards merging of the localized shear zone with seismogenic faults, in which case frictional melt generation could result.

A potentially important observation linking GBS with pseudotachylyte formation is a microstructure common to both plastic instabilities and GBS. The ductile fracture of large grains accompanies the acceleration of strain rate (Shigematsu et al., 2004), but a lower strain precursor to ductile rupture is cavitation in fine-grained aggregates (Rybacki et al., 2008), which is also observed in fine-grained materials undergoing GBS (e.g., Zavada et al., 2007; Rybacki et al., 2010; Menegon et al., 2015). Fluids play a key role in promoting cavitation during GBS, and may also facilitate deep seismicity (e.g., Rybacki et al., 2010). Similarly, fluid-assisted GBS may have led to accelerated strain rates within the fine-grained quartz from which pseudotachylyte was generated, rendering the precursor to the pseudotachylyte weaker than the minimally disaggregated polycrystalline survivor clasts within it. Fluids were likely present in footwall rocks based on the presence of fluid

inclusions (Smith et al., 1991) and hydrous phases such as biotite (Reynolds, 1985); the presence of grain boundary fluid is suggested by the fine grains of interstitial biotite between quartz grains in polycrystalline survivor clasts. This is also consistent with the work of Goodwin (1999), who invokes the presence of hydrous biotite along C-planes to explain the generation of pseudotachylyte in particular.

The presence of fluid is also important for enhancing the operation of diffusion creep at the temperature and stress conditions associated with mylonite and pseudotachylyte development. The *c*-axis patterns of quartz are consistent with temperatures over the range ~400-500°C, based on correlation with experimental results (e.g., Stipp et al., 2002; Stipp et al., 2010; Law, 2014). The large range in temperatures reflects the sensitivity of fabric development to strain rate, stress, and fluid activity (Law, 2014), so it is difficult to correlate the *c*-axis patterns with specific temperatures. An additional constraint on temperature is provided by the simultaneous brittle deformation of feldspars and plastic deformation of quartz; these microstructures indicate temperatures near the onset of feldspar plasticity (e.g., Simpson, 1985; Tullis et al., 1990). However, the *c*-axis fabrics and feldspar microstructures both indicate much lower temperatures than what are commonly associated with diffusion creep in quartz (e.g., Rutter and Brodie, 2004).

The addition of fluids during diffusion creep may reconcile this temperature discrepancy; wet feldspar aggregates show an expanded field of diffusion creep in experimental deformation mechanism maps (Rybacki and Dresen, 2004), and the diffusion of Si in quartz is enhanced by fluid (Farver and Yund, 2000). Other studies of naturally deformed rocks also note a discrepancy between the conditions under which they interpret

diffusion creep in quartz and those indicated by experimental quartz data (e.g., Kilian et al., 2011; Okudaira and Shigematsu, 2012; Rahl and Skemer, 2016). We suspect that in the South Mountains, pulses of magmatic fluid (Smith et al., 1991) channeling into zones of GBS enhanced diffusion creep, promoted cavitation, and led to local bursts of strain rate acceleration and subsequent pseudotachylyte formation. This process is likely cyclic, as field observations demonstrate multiple generations of pseudotachylyte (Goodwin, 1999). In other studies (White, 2012 and references therein) the cyclicity of pseudotachylyte development in the deep crust has been explained through plastic instabilities that give rise to periodic bursts of dislocation glide, and these workers note how the cyclic phenomenon is similar to the episodicity surrounding tremor events at depth. In the case of the South Mountains pseudotachylytes, we suspect that tremor-like events may have occurred periodically by the pulsing of magmatic fluids into localized shear zones deformed by GBS, triggering an acceleration of strain rate and the formation of pseudotachylyte. Subsequent flow within pseudotachylytes is accommodated by melt, until cooling and crystallization promotes an increase in strength of the pseudotachylyte (e.g., Goodwin, 1999; Rowe and Griffith, 2015; Mitchell et al., 2016) and motion is arrested.

The South Mountains pseudotachylytes preserve details of interseismic and coseismic deformation, but they do not show evidence for postseismic stress relaxation. The ‘control’ mylonite, host mylonite, and pseudotachylyte show increasing values of stress rather than decreasing stress associated with stress relaxation (Trepmann and Stockhert, 2013). The high stresses associated with both host mylonite and pseudotachylyte veins could either represent high interseismic stresses at the base of the BDT, or the stress pulses associated with the tip of a downward propagating rupture, in which case the host

mylonite and pseudotachylyte record stresses associated with interseismic and coseismic deformation, respectively. We explain the absence of postseismic stress relaxation as being a product of fast footwall denudation, as the slip rate associated with the South Mountains brittle detachment was ~ 0.3 cm/yr (Fitzgerald et al., 1993). The fast denudation and attendant cooling suppressed grain growth and grain boundary mobility that would accommodate postseismic relaxation. We conclude that denudation of footwall rocks during normal faulting is therefore likely to preserve pseudotachylytes created at depth, but their removal from depth and transport above the long-term BDT prevents them from recording postseismic stress relaxation.

Chapter 6: Conclusions

We have used EBSD analyses to investigate mylonite-hosted pseudotachylyte formation in the footwall of an extensional core complex and to relate its formation to the seismic cycle. Like previous studies of pseudotachylyte from the South Mountains (Goodwin, 1999), we also find that grain size sensitive flow was a key part of pseudotachylyte development, but our EBSD data allow us to take a step further and investigate the grain-scale processes that accommodated grain size sensitive flow. We summarize our results as follows:

- Dynamic recrystallization of quartz is accommodated first by SGR and then by BLG, leading to progressive grain size reduction along the quartz piezometer during dislocation creep.
- The reduction in grain size leads to a change in deformation mechanism, resulting in a decrease in effective viscosity and an acceleration of strain rate that promotes the onset of GBS associated with diffusion creep.
- The transition in deformation mechanism promotes strain localization within zones deforming by GBS. Pseudotachylytes subsequently nucleate within these zones, aided by runaway strain rates and the infiltration of fluids that enhance diffusion creep and GBS.
- The high stresses in the host mylonite and pseudotachylyte are most likely associated with high ambient stresses in the upper part of the BDT, which is consistent with either *in situ* and coeval formation of pseudotachylyte within

mylonites, or the potential for a ‘bottom-up’ stress transfer upwards towards weaker brittle faults within the seismogenic zone.

- Pseudotachylyte may form periodically from pulses of fluid-assisted diffusion creep and GBS in association with deep tremor events.
- Mylonite-hosted coeval pseudotachylytes in extensional settings are likely to record stresses associated with interseismic and coseismic deformation, but progressive denudation of footwall rocks from beneath the BDT removes the pseudotachylytes from structural depths from which they are likely to record stress relaxation associated with postseismic deformation.

References:

- Annis, D., 2012. EBSD and Microstructural Analysis of Quartzofeldspathic rocks from the South Mountains, Arizona: an Evaluation of flow laws and Crustal Rheology. M.Sc. thesis, California State University Northridge.
- Ashby, M.F., Verrall, R.A., 1973. Diffusion-accommodated flow and superplasticity. *Acta Metall.* 21, 149–163. doi:10.1016/0001-6160(73)90057-6
- Behr, W.M., Platt, J.P., 2014. Brittle faults are weak, yet the ductile middle crust is strong: Implications for lithospheric mechanics. *Geophys. Res. Lett.* 41, 8067–8075. doi:10.1002/2014GL061349
- Bestmann, M., Pennacchioni, G., Frank, G., Göken, M., de Wall, H., 2011. Pseudotachylyte in muscovite-bearing quartzite: Coseismic friction-induced melting and plastic deformation of quartz. *J. Struct. Geol.* 33, 169–186. doi:10.1016/j.jsg.2010.10.009
- Bestmann, M., Prior, D.J., 2003. Intragranular dynamic recrystallization in naturally deformed calcite marble: Diffusion accommodated grain boundary sliding as a result of subgrain rotation recrystallization. *J. Struct. Geol.* 25, 1597–1613. doi:10.1016/S0191-8141(03)00006-3
- Bürgmann, R., Dresen, G., 2008. Rheology of the lower crust and upper mantle: Evidence from rock mechanics, geodesy, and field observations. *Annu. Rev. Earth Planet. Sci.* 36, 531–567. doi:10.1146/annurev.earth.36.031207.124326
- Clements, B., Schwartz, J., Miranda, E., 2013. U-Pb geochronology of the south mountains metamorphic core complex, central Arizona. *Geological Society of America Abstracts with Programs*. Vol. 45, No. 7, p.763.
- Czaplińska, D., Piazzolo, S., Zibra, I., 2015. The influence of phase and grain size distribution on the dynamics of strain localization in polymineralic rocks. *J. Struct. Geol.* 72, 15–32. doi:10.1016/j.jsg.2015.01.001
- De Bresser, J.H.P., Ter Heege, J.H., Spiers, C.J., 2001. Grain size reduction by dynamic recrystallization: Can it result in major rheological weakening? *Int. J. Earth Sci.* 90, 28–45. doi:10.1007/s005310000149
- Ellis, S., Stockhert, B., 2004. Elevated stresses and creep rates beneath the brittle-ductile transition caused by seismic faulting in the upper crust. *J. Geophys. Res. Solid Earth* 109, 1–10. doi:10.1029/2003JB002744
- Farver, J., Yund, R., 2000. Silicon diffusion in a natural quartz aggregate: constraints on solution-transfer diffusion creep. *Tectonophysics* 325, 193–205. doi:10.1016/S0040-1951(00)00121-9

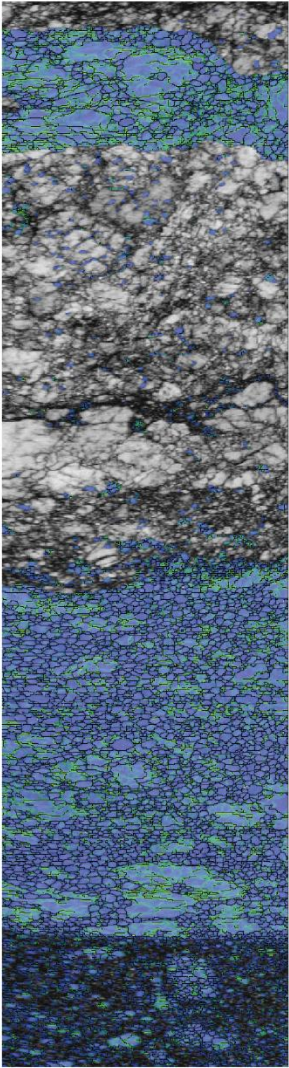
- Fitzgerald, P.G., Reynolds, S.J., Stump, E., Foster, D.A., Gleadow, A.J.W., 1993. Thermochronologic evidence for timing of denudation and rate of crustal extension of the south mountains metamorphic core complex and sierra estrella, Arizona. *Nucl. Tracks Radiat. Meas.* 21, 555–563. doi:10.1016/1359-0189(93)90196-G
- Fressengeas, C., Molinari, A., 1987. Instability and localization of plastic flow in shear at high strain rates. *Journal of the Mechanics and Physics of Solids* 35, 185e211.
- Goodwin, L.B., 1999. Controls on pseudotachylite formation during tectonic exhumation in the South Mountains metamorphic core complex, Arizona. *Geol. Soc. London, Spec. Publ.* 154, 325–342. doi:10.1144/GSL.SP.1999.154.01.15
- Greenberg, R.M., 2010. Strain localization in quartzofeldspathic mylonites: a microstructural and electron backscatter diffraction (EBSD) study of the South Mountains Core Complex, Arizona. M.Sc. thesis, California State University Northridge.
- Gueydan, F., Leroy, Y.M., Jolivet, L., 2001. Grain-size-sensitive flow and shear-stress enhancement at the brittle-ductile transition of the continental crust. *Int. J. Earth Sci.* 90, 181–196. doi:10.1007/s005310000160
- Halfpenny, A., Prior, D.J., Wheeler, J., 2012. Electron backscatter diffraction analysis to determine the mechanisms that operated during dynamic recrystallisation of quartz-rich rocks. *J. Struct. Geol.* 36, 2–15. doi:10.1016/j.jsg.2012.01.001
- Halfpenny, A., Prior, D.J., Wheeler, J., 2006. Analysis of dynamic recrystallization and nucleation in a quartzite mylonite. *Tectonophysics* 427, 3–14. doi:10.1016/j.tecto.2006.05.016
- Heilbronner, R., Tullis, J., 2006. Evolution of c axis pole figures and grain size during dynamic recrystallization: Results from experimentally sheared quartzite. *J. Geophys. Res.* 111, B10202. doi:10.1029/2005JB004194
- Herwegh, M., Linckens, J., Ebert, A., Berger, A., Brodhag, S.H., 2011. The role of second phases for controlling microstructural evolution in polymineralic rocks: A review. *J. Struct. Geol.* 33, 1728–1750. doi:10.1016/j.jsg.2011.08.011
- Hirth, G., Teyssier, C., Dunlap, W.J., 2001. An evaluation of quartzite flow laws based on comparisons between experimentally and naturally deformed rocks. *Int. J. Earth Sci.* 90, 77–87. doi:10.1007/s005310000152
- Hirth, G., Tullis, J., 1992. Dislocation creep regimes in quartz aggregates. *J. Struct. Geol.* 14, 145–159. doi:10.1016/0191-8141(92)90053-Y
- Humphreys, F.J., 2001. Grain and subgrain characterisation by electron backscatter diffraction. *J. Mater. Sci.* 36, 3833–3854. doi:10.1023/A:1017973432592

- Kilian, R., Heilbronner, R., Stünitz, H., 2011. Quartz grain size reduction in a granitoid rock and the transition from dislocation to diffusion creep. *J. Struct. Geol.* 33, 1265–1284. doi:10.1016/j.jsg.2011.05.004
- Kirkpatrick, J.D., Rowe, C.D., 2013. Disappearing ink: How pseudotachylytes are lost from the rock record. *J. Struct. Geol.* 52, 183–198. doi:10.1016/j.jsg.2013.03.003
- Law, R.D., Mainprice, D., Casey, M., Lloyd, G.E., Knipe, R.J., Cook, B., Thigpen, J.R., 2010. Moine Thrust zone mylonites at the Stack of Glencoul: I – microstructures, strain and influence of recrystallization on quartz crystal fabric development. *Geol. Soc. London, Spec. Publ.* 335, 543–577. doi:10.1144/SP335.23
- Law, R.D., 2014. Deformation thermometry based on quartz c-axis fabrics and recrystallization microstructures: A review. *J. Struct. Geol.* 66, 129–161. doi:10.1016/j.jsg.2014.05.023
- Linckens, J., Herwegh, M., Müntener, O., Mercolli, I., 2011. Evolution of a polymineralic mantle shear zone and the role of second phases in the localization of deformation. *J. Geophys. Res. Solid Earth* 116, 1–21. doi:10.1029/2010JB008119
- Linckens, J., Herwegh, M., Müntener, O., 2015. Small quantity but large effect - How minor phases control strain localization in upper mantle shear zones. *Tectonophysics* 643, 26–43. doi:10.1016/j.tecto.2014.12.008
- Linder, A., 2015. Timing of mid-crustal deformation with respect to magmatism and detachment faulting in the South Mountains metamorphic core complex, Arizona, USA. Undergraduate Senior Thesis, California State University Northridge.
- Livaccari, R.F., Geissman, J.W., Reynolds, S.J., 1995. Large-magnitude extensional deformation in the South Mountains metamorphic core complex, Arizona: evaluation with paleomagnetism. *Geol. Soc. Am. Bull.* 107, 877–894. doi:10.1130/0016-7606(1995)107<0877:LMEDIT>2.3.CO;2
- Mainprice, D., Jaoul, O., 2009. A transmission electron microscopy study of experimentally deformed quartzite with different degrees of doping. *Phys. Earth Planet. Inter.* 172, 55–66. doi:10.1016/j.pepi.2008.07.009
- Mariani, E., Prior, D., 2009. Microstructure Evolution during Creep and Annealing of Minerals and Rocks. *Microsc.* 15, 412–413. doi:10.1017/S14319276090962
- Menegon, L., Fusses, F., Stunitz, H., Xiao, X., 2015. Creep cavitation bands control porosity and fluid flow in lower crustal shear zones. *Geology* 43, 227–230. doi:10.1130/G36307.1
- Mitchell, T.M., Toy, V., Di Toro, G., Renner, J., Sibson, R.H., 2016. Fault welding by pseudotachylyte formation. *Geology* G38373.1. doi:10.1130/G38373.1

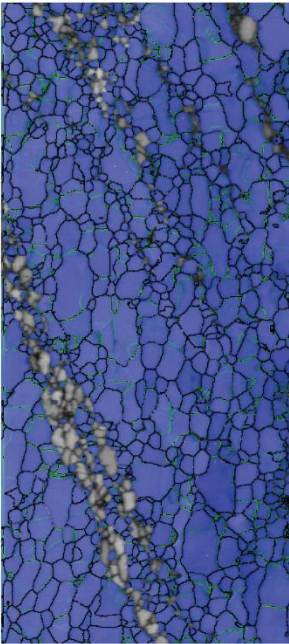
- Okudaira, T., Shigematsu, N., 2012. Estimates of stress and strain rate in mylonites based on the boundary between the fields of grain-size sensitive and insensitive creep. *J. Geophys. Res. Solid Earth* 117. doi:10.1029/2011JB008799
- Oliot, E., Goncalves, P., Schulmann, K., Marquer, D., Lexa, O., 2014. Mid-crustal shear zone formation in granitic rocks: Constraints from quantitative textural and crystallographic preferred orientations analyses. *Tectonophysics* 612–613, 63–80. doi:10.1016/j.tecto.2013.11.032
- Platt, J.P., Behr, W.M., 2011. Lithospheric shear zones as constant stress experiments. *Geology* 39, 127–130. doi:10.1130/G31561.1
- Platt, J.P., Behr, W.M., Cooper, F.J., 2014. Metamorphic core complexes: windows into the mechanics and rheology of the crust. *J. Geol. Soc. London.* 172, 9–27. doi:10.1144/jgs2014-036
- Platt, J.P., 2015. Rheology of two-phase systems: A microphysical and observational approach. *J. Struct. Geol.* 77, 213–227. doi:10.1016/j.jsg.2015.05.003
- Price, N.A., Johnson, S.E., Gerbi, C.C., West, D.P., 2012. Identifying deformed pseudotachylyte and its influence on the strength and evolution of a crustal shear zone at the base of the seismogenic zone. *Tectonophysics* 518–521, 63–83. doi:10.1016/j.tecto.2011.11.011
- Rahl, J.M., Skemer, P., 2016. Microstructural evolution and rheology of quartz in a mid-crustal shear zone. *Tectonophysics* 680, 129–139. doi:10.1016/j.tecto.2016.05.022
- Reynolds, S.J., 1985. Geology of the South Mountains, Central Arizona. *Arizona Geol. Surv. Bull.* 195, 75.
- Reynolds, S.J., Shafiqullah, M., Damon, P.E., Dewitt, E., 1986. Early Miocene mylonitization and detachment faulting, South Mountains, central Arizona 283–286.
- Rowe, C.D., Griffith, W.A., 2015. Do faults preserve a record of seismic slip: A second opinion. *J. Struct. Geol.* 78, 1–26. doi:10.1016/j.jsg.2015.06.006
- Rutter, E.H., Brodie, K.H., 2004. Experimental grain size-sensitive flow of hot-pressed Brazilian quartz aggregates. *J. Struct. Geol.* 26, 2011–2023. doi:10.1016/j.jsg.2004.04.006
- Rybacki, E., Dresen, G., 2004. Deformation mechanism maps for feldspar rocks. *Tectonophysics* 382, 173–187. doi:10.1016/j.tecto.2004.01.006
- Rybacki, E., Wirth, R., Dresen, G., 2010. Superplasticity and ductile fracture of synthetic feldspar deformed to large strain. *J. Geophys. Res.* 115, B08209. doi:10.1029/2009JB007203

- Rybacki, E., Wirth, R., Dresen, G., 2008. High-strain creep of feldspar rocks: Implications for cavitation and ductile failure in the lower crust. *Geophys. Res. Lett.* 35, 1–5. doi:10.1029/2007GL032478
- Scholz, C. H., 2002, *The mechanics of earthquakes and faulting*, 2nd Edn., Cambridge University press, Cambridge.
- Shigematsu, N., Fujimoto, K., Ohtani, T., Goto, K., 2004. Ductile fracture of fine-grained plagioclase in the brittle-plastic transition regime: Implication for earthquake source nucleation. *Earth Planet. Sci. Lett.* 222, 1007–1022. doi:10.1016/j.epsl.2004.04.001
- Sibson, R.H., 1980. Transient discontinuities in ductile shear zones. *J. Struct. Geol.* 2, 165–171. doi:10.1016/0191-8141(80)90047-4
- Sibson, R.H., 1983. Continental fault structure and the shallow earthquake source. *J. Geol. Soc. London.* 140, 741–767. doi:10.1144/gsjgs.140.5.0741
- Simpson, C., 1985. Deformation of granitic rocks across the brittle-ductile transition. *J. Struct. Geol.* 7, 503–511. doi:10.1016/0191-8141(85)90023-9
- Skemer, P., Karato, S.I., 2008. Sheared lherzolite xenoliths revisited. *J. Geophys. Res. Solid Earth* 113, 1–14. doi:10.1029/2007JB005286
- Smith, B.M., Reynolds, S.J., Day, H.W., Bodnar, R.J., 1991. Deep-seated fluid involvement in ductile-brittle deformation and mineralization, South Mountains metamorphic core complex, Arizona. *Geol. Soc. Am. Bull.* 103, 559–569. doi:10.1130/0016-7606(1991)103<0559:DSFIID>2.3.CO;2
- Stipp, M., Stunitz, H., Heilbronner, R., Schmid, S.M., 2002. Dynamic recrystallization of quartz: correlation between natural and experimental conditions. *Geol. Soc. London, Spec. Publ.* 200, 171–190. doi:10.1144/GSL.SP.2001.200.01.11
- Stipp, M., Stünitz, H., Heilbronner, R., Schmid, S.M., 2002. The eastern Tonale fault zone: A “natural laboratory” for crystal plastic deformation of quartz over a temperature range from 250 to 700 °C. *J. Struct. Geol.* 24, 1861–1884. doi:10.1016/S0191-8141(02)00035-4
- Stipp, M., Tullis, J., 2003. The recrystallized grain size piezometer for quartz. *Geophys. Res. Lett.* 30, 2088. doi:10.1029/2003GL018444
- Stipp, M., Tullis, J., Scherwath, M., Behrmann, J.H., 2010. A new perspective on paleopiezometry: Dynamically recrystallized grain size distributions indicate mechanism changes. *Geology* 38, 759–762. doi:10.1130/G31162.1
- Trepmann, C.A., Stöckhert, B., 2013. Short-wavelength undulatory extinction in quartz recording coseismic deformation in the middle crust; An experimental study. *Solid Earth* 4, 263–276. doi:10.5194/se-4-263-2013

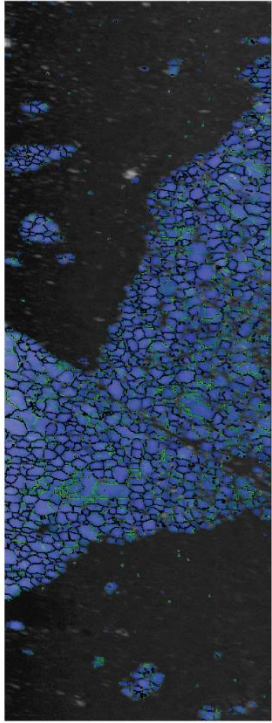
- Tullis, J., Dell'Angelo, L., Yund, R.A., 1990. Ductile shear zones from brittle precursors in feldspathic rocks: The role of dynamic recrystallization. American Geophysical Union, pp. 67–81. doi:10.1029/GM056p0067
- Wheeler, J., 2009. The preservation of seismic anisotropy in the Earth's mantle during diffusion creep. *Geophys. J. Int.* 178 (3), 1723–1732.
- Wehrens, P., Berger, A., Peters, M., Spillmann, T., Herwegh, M., 2016. Deformation at the frictional-viscous transition: Evidence for cycles of fluid-assisted embrittlement and ductile deformation in the granitoid crust. *Tectonophysics* 693, 66–84. doi:10.1016/j.tecto.2016.10.022
- White, J.C., 2012. Paradoxical pseudotachylyte – Fault melt outside the seismogenic zone. *J. Struct. Geol.* 38, 11–20. doi:10.1016/j.jsg.2011.11.016
- White, J.C., 1996. Transient discontinuities revisited: pseudotachylyte, plastic instability and the influence of low pore fluid pressure on deformation processes in the mid-crust. *J. Struct. Geol.* 18, 1471–1486. doi:10.1016/S0191-8141(96)00059-4
- White, S., 1979. Grain and sub-grain size variations across a mylonite zone. *Contrib. to Mineral. Petrol.* 70, 193–202. doi:10.1007/BF00374448
- Závada, P., Schulmann, K., Konopásek, J., Ulrich, S., Lexa, O., 2007. Extreme ductility of feldspar aggregates - Melt-enhanced grain boundary sliding and creep failure: Rheological implications for felsic lower crust. *J. Geophys. Res. Solid Earth* 112, 1–15. doi:10.1029/2006JB004820
- Zhang, Y., Hobbs, B.E., Jessell, M.W., 1994. The effect of grain-boundary sliding on fabric development in polycrystalline aggregates. *J. Struct. Geol.* 16, 1315–1325. doi:10.1016/0191-8141(94)90072-8



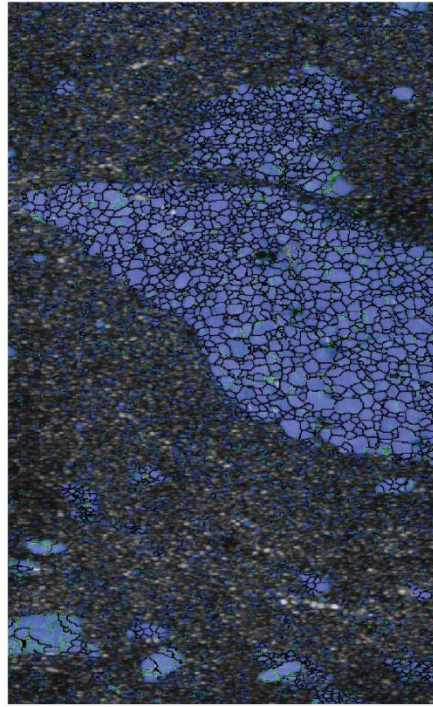
200 μm



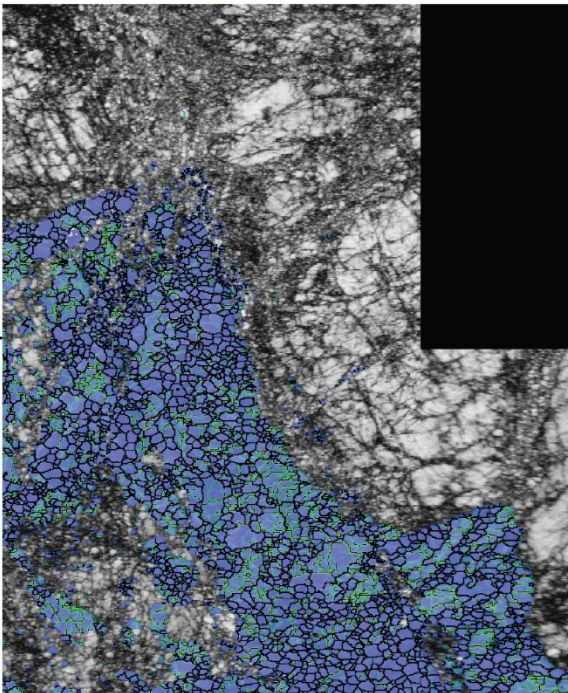
100 μm



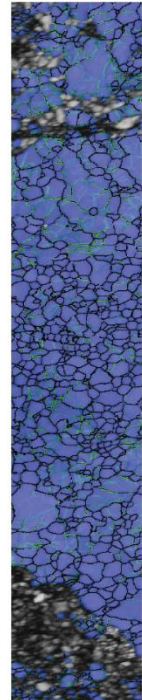
100 μm



50 μm

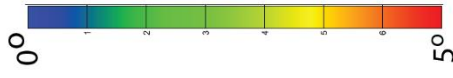


200 μm



100 μm

Local quartz miso.



Appendix A